



Denudation of the Cordillera and intraplate belt in Central Patagonia inferred by detrital multi-dating of foreland basin deposits

Marie Genge, Massimiliano Zattin, César Witt, Alexis Derycke, Cécile Gautheron, Stefano Mazzoli, Maurizio Petrelli, Nathan Cogné, Delphine Bosch, Olivier Bruguier, et al.

► To cite this version:

Marie Genge, Massimiliano Zattin, César Witt, Alexis Derycke, Cécile Gautheron, et al.. Denudation of the Cordillera and intraplate belt in Central Patagonia inferred by detrital multi-dating of foreland basin deposits. *Sedimentary Geology*, 2022, 440, pp.106237. 10.1016/j.sedgeo.2022.106237 . insu-03765253

HAL Id: insu-03765253

<https://insu.hal.science/insu-03765253>

Submitted on 31 Aug 2022

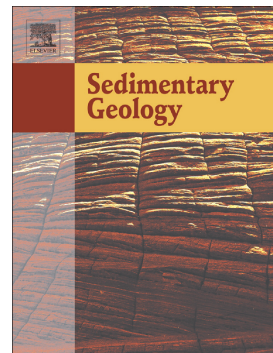
HAL is a multi-disciplinary open access archive for the deposit and dissemination of scientific research documents, whether they are published or not. The documents may come from teaching and research institutions in France or abroad, or from public or private research centers.

L'archive ouverte pluridisciplinaire **HAL**, est destinée au dépôt et à la diffusion de documents scientifiques de niveau recherche, publiés ou non, émanant des établissements d'enseignement et de recherche français ou étrangers, des laboratoires publics ou privés.

Journal Pre-proof

Denudation of the Cordillera and intraplate belt in Central Patagonia inferred by detrital multi-dating of foreland basin deposits

Marie C. Genge, Massimiliano Zattin, César Witt, Alexis Derycke, Cécile Gautheron, Stefano Mazzoli, Maurizio Petrelli, Nathan Cogné, Delphine Bosch, Olivier Bruguier, Marcelo Marquez



PII: S0037-0738(22)00158-0

DOI: <https://doi.org/10.1016/j.sedgeo.2022.106237>

Reference: SEDGEO 106237

To appear in: *Sedimentary Geology*

Received date: 6 July 2022

Revised date: 20 August 2022

Accepted date: 21 August 2022

Please cite this article as: M.C. Genge, M. Zattin, C. Witt, et al., Denudation of the Cordillera and intraplate belt in Central Patagonia inferred by detrital multi-dating of foreland basin deposits, *Sedimentary Geology* (2022), <https://doi.org/10.1016/j.sedgeo.2022.106237>

This is a PDF file of an article that has undergone enhancements after acceptance, such as the addition of a cover page and metadata, and formatting for readability, but it is not yet the definitive version of record. This version will undergo additional copyediting, typesetting and review before it is published in its final form, but we are providing this version to give early visibility of the article. Please note that, during the production process, errors may be discovered which could affect the content, and all legal disclaimers that apply to the journal pertain.

Denudation of the Cordillera and intraplate belt in central Patagonia inferred by detrital multi-dating of foreland basin deposits

Marie C. Genge^{1,2*}, Massimiliano Zattin¹, César Witt², Alexis Derycke^{3,4}, Cécile Gautheron³, Stefano Mazzoli⁵, Maurizio Petrelli⁶, Nathan Cogné⁴, Delphine Bosch⁷, Olivier Bruguier⁷, Marcelo Marquez⁸

¹ Dipartimento di Geoscienze, Università degli Studi di Padova, Italy

² Univ. Lille, CNRS, IRD, Univ. Littoral Côte d'Opale, UMR 8187, LOG, Laboratoire d'Océanologie et de Géosciences, F 59000 Lille, France

³ Université Paris-Saclay, CNRS, GEOPS, 91405, Orsay, France

⁴ Univ. Rennes, CNRS, Géosciences Rennes, UMR 6118, 35000, Rennes, France

⁵ School of Science and Technology, Geology Division, University of Camerino, Italy

⁶ Department of Physics and Geology, University of Perugia, Perugia, Italy

⁷ Geosciences Montpellier, CNRS UMR-5243, Université Montpellier II, 34095, Montpellier, France

⁸ Servicio Geológico Mineo-Argentino, Delegación Patagonia, Barrio Don Bosco km 8, Comodoro Rivadavia, Argentina

*corresponding author: mcgenge@hku.hk

Abstract

The evolution of central Patagonia is associated with episodic shortening and extension that have greatly affected the topography of the Cordillera and intraplate belt. The San Jorge Basin is a site of sediment accumulation in the foreland that is surrounded by igneous and broken foreland relief. The latter originated from episodic deformation and reactivation of inherited structures associated with a period of slab shallowing that allowed the far-field transmission of Andean stresses to the foreland. Thus, due to of its location, the San Jorge Basin provides an exceptional opportunity to study the denudation of both Cordilleran and intraplate topography during the Cenozoic, particularly during the late Eocene–early Miocene interval of mild deformation. In this study, we use a single-grain geochronological approach combining apatite fission tracks and U–Pb dating on apatite, along with maximum deposition ages obtained from U–Pb zircon dating for Neogene foreland basin deposits, to distinguish between two distinctive sediment source regions in central Patagonia during the Cenozoic, despite the persistent volcanic signal. A compilation of previously published cooling ages combined with our new data define: (i) a dominant local source from the northern broken foreland from the late Eocene until the early Miocene; and (ii) a widespread source in the Cordillera during the Miocene based on a very uniform thermochronological signal observed throughout the entire foreland. Therefore, this study provides new insights into the variation of in sediment sourcing in the central Patagonian foreland. This variation is primarily controlled by the decrease of post-orogenic erosional processes during a period of relative tectonic quiescence following the highly active Early Cretaceous–middle Eocene time interval.

Keywords: foreland basin; provenance; apatite fission track; apatite and zircon U–Pb; central Patagonia

1 Introduction

The modern Andean foreland basin represents an elongated trough on the eastern (i.e., retro-wedge) side of the Andean Cordillera and is the product of flexural subsidence driven by the loading from orogenic crustal thickening (e.g., Jordan et al., 1982; DeCelles and Giles, 1996). In central Patagonia, the San Jorge Basin is a deep depocenter located far from the orogen and bounded by the broken foreland. The latter refers to a series of structural highs that are believed to have developed by the reactivation of extensional structures, inherited from the break-up of Western Gondwana (Mpodozis and Ramos, 2008; Figari et al., 2016). Deformation occurred during a Cretaceous – middle Eocene contractional phase (e.g., Homovc et al., 1995; Marquez and Navarrete, 2015; Echaurren et al., 2017) that may have resulted from fluctuations in slab dynamics (mostly from steep to gently dipping or flat-slab subduction; e.g., Savignano et al., 2016; Horton, 2018). The decrease of slab dip angle may have allowed far-field stresses to propagate throughout the entire foreland. Horizontal E–W shortening and extension perpendicular to it resulted in the development of the roughly N–S striking broken foreland reliefs of the San Bernardo Fold and Thrust Belt (FTB) and the E–W elongated trough of the San Jorge Basin, which is mostly controlled by the reactivation of ~E–W striking structures (Foix et al., 2012; Ramos, 2014; Gianni et al., 2015b). The following period was characterized by a general subsidence related to slab-rollback until the middle Miocene. Later, changes in plate convergence led to a new contractional phase mostly affecting the Cordillera (e.g., Orts et al., 2012, 2015; Bechis et al., 2014; Encinas et al., 2014;

Echaurren et al., 2016) and to a lesser extent the broken foreland (e.g., Savignano et al., 2016; Fernández et al., 2020).

In this context, the San Jorge Basin is very likely to record the complex Cenozoic history of central Patagonia. The San Jorge Basin is surrounded by the central Patagonian Andes to the west, the San Bernardo FTB and the North Patagonian Massif to the north, and the Deseado Massif (a large basement province) to the south (Figure 1). These reliefs represent the main topographic features of the central Patagonian foreland, and thus are potential sources of sediments, as evidenced by Late Cretaceous deposits in the southern San Jorge Basin derived from the Deseado Massif (Limarino and Giordano, 2016). However, although the structural evolution of these features and their relationships with the adjacent foreland basin are relatively well studied (e.g., Allard et al., 2020), the source-to-sink scenarios in this section of Patagonia during the Cenozoic remain elusive. Understanding these scenarios is fundamental to unravel the denudation history of the Patagonian reliefs. Within this context, the San Jorge Basin represents an exceptional natural laboratory for provenance analysis because the erosion products of the Cordillera and intraplate belt can be expected to be readily distinguishable due to different cooling periods. Indeed, iN-Situ thermochronological studies, mostly apatite fission tracks (^{40}FT) and (U-Th)/He (AHe) dating, indicate a wide range of cooling ages spanning from the Cretaceous to the Miocene across the Cordillera. On the other hand, only Cretaceous – early Paleogene ages have been recognized at the Deseado Massif and the southwestern San Bernardo FTB (Figure 1) (Fernández et al., 2020; Genge et al., 2021a). Furthermore, the moderate thickness of the Cenozoic sedimentary cover, which is < 1 km even in the basin center (Figari et al., 1999), prevents of any thermal reset of the data. The sedimentary rocks exposed in the San Jorge Basin thus may provide information about the long-term exhumation of the source rocks, although the substantial Andean volcanic input in this area represents a major challenge to unraveling the exhumation history of source rocks.

(Paredes et al., 2009; Umazano et al., 2009; Allard et al., 2020; Foix et al., 2020). Multi-dating on a single-phase (apatite in this case) provides a key tool for addressing this challenge, as medium-temperature data reveal the time of crystallization whereas low-temperature data are related to cooling ages at shallow depths, thus allowing us to discriminate between volcanic and exhumation signals (e.g., Saylor et al., 2012; Malusà et al., 2022).

This work presents new U–Pb and fission tracks dating of detrital apatite and U–Pb dating of detrital zircons that were collected from lower Eocene to middle Miocene sedimentary successions exposed in the proximal (Andean foothill) and distal (Atlantic coast) areas of the San Jorge Basin. These data were integrated with published low-temperature cooling ages (Genge et al., 2021a) and new geochronological data obtained on Cretaceous samples from the San Bernardo FTB (this study). The combined dataset, besides providing new geochronological constraints for Miocene deposits, demonstrates that the sediment sources (volcanic input aside) changed through time. Sedimentary materials were derived from both distant (i.e., the Andean Cordillera) and local (i.e., the San Bernardo FTB) sources. Thus, our provenance analysis sheds new light into the denudation of central Patagonian reliefs and their relationship with orogen dynamics. In addition, we demonstrate the potential of using multi-technique approaches to distinguish syn-volcanic inputs among sediment sources and unravel the relative contribution of recycling processes.

2 Regional geological setting

The current geodynamic configuration of central Patagonia is governed by the subduction of the oceanic Nazca and Antarctic plates beneath the continental South American Plate (Figures

1 and 2). Central Patagonia (44 – 48 °S) is the transitional zone between northern and austral Patagonia. This region is coincident with the Chile Triple Junction at around 46°30' S, where the Chilean Ridge segment, which separates the Nazca and Antarctic plates, is currently being subducted beneath the South American Plate (e.g., Cande and Leslie, 1986). The northward migration of the Chile Triple Junction (from 54°S to 46°S) over the past 14 m.y. resulted in the opening of a slab window below the whole austral Patagonia (e.g., Breitsprecher and Thorkelson, 2009; Scalabrino et al., 2009).

Compared to other sectors of the Andean Cordillera, the central Patagonian Andes are characterized by lower elevations, thinner crust and a narrow width (Mpodozis and Ramos, 2008; Orts et al., 2012). The San Jorge Basin (Figures 1 and 2) is a broadly E–W elongated, on-shore-off-shore basin related to extensional processes, while the Patagonia region experienced mostly shortening during the Mesozoic–Cenozoic (e.g., Folguera et al., 2020). This extension basin is bounded by the igneous-metamorphic province known as the Deseado Massif in the south (e.g., Giacosa et al., 2010), the North Patagonian Massif in the north, and the San Bernardo FTB in the northwest. The latter consists of Mesozoic sedimentary successions originally deposited in grabens that formed during the break-up of the Gondwana paleocontinent (Fitzgerald et al., 1990; Mpodozis and Ramos, 2008; Figari et al., 2016) and have been episodically deformed since the late Early Cretaceous (Homovc et al., 1995; Gianni et al., 2015a). The development of this NNW–SSE-trending intraplate belt, which is a part of the broken foreland, resulted in the disconnection of the eastern San Jorge Basin and the Río Mayo sub-basin, another Mesozoic basin located along the eastern side of the current Cordillera (Homovc et al., 1995; Peroni et al., 1995; Figari et al., 1999; Navarrete et al., 2015). Low-temperature thermochronological data suggest that the San Bernardo FTB mostly developed during the late Early Cretaceous to early Paleogene, as no significant cooling has been recorded in the Neogene (Savignano et al., 2016; Genge et al., 2021b), aside from areas

affected by long-term volcanism (Genge et al., 2021a). Finally, minor to moderate deformation affected the broken foreland during the Neogene and the Quaternary as evidenced by the local folding of Oligocene basaltic layers, growth strata in surface and subsurface data, and late reactivation of inherited normal faults (e.g., Gianni et al., 2015a; Gianni et al., 2017).

2.1 Stratigraphy

The sedimentary successions of the San Jorge Basin were deposited above Paleozoic to Triassic intrusive and metamorphic basement rocks that are currently exposed in the Deseado Massif (Lesta et al., 1980; Ramos, 2008). This basement was faulted during back-arc extension and the break-up of Gondwana during the Jurassic to Early Cretaceous (Suarez and Marquez, 2007; Mpodozis and Ramos, 2008; Figari et al., 2016). Directly overlying the basement, syn-extensional Jurassic – Lower Cretaceous deposits can be grouped into several lithostratigraphic units (Figure 3) based on their volcanic content and geographic location (e.g., Fitzgerald et al., 1990; Figari et al., 1999, 2002; Pankhurst et al., 1999; Sylwan, 2001; Suarez and Marquez, 2007; Lloyd et al., 2020).

At the top of the Jurassic–Lower Cretaceous deposits, a major unconformity is observed regionally, and is related to E–W shortening associated with slab shallowing in the late Early Cretaceous to early Paleogene (Navarrete et al., 2016, 2018; Horton, 2018), eventually evolving to a flat slab during the Late Cretaceous (Gianni et al., 2018). This E–W shortening affected the whole central Patagonia as indicated by the syn-orogenic character of the Cretaceous continental Chubut Group. The latter, being mainly exposed across the San Bernardo FTB (Figure 2), is generally characterized by a high proportion of volcaniclastic

supply (Lesta and Ferello, 1972; Clavijo, 1986; Homovc et al., 1995; Tunik et al., 2004; U�azano et al., 2012; Gianni et al., 2015a; Navarrete et al., 2015; Allard et al., 2020).

The continental Chubut Group is locally covered by transitional to unconformable marine successions of the Danian Salamanca Formation (Figure 3; Lesta and Ferello, 1972; Bellosi et al., 2000; Clyde et al., 2014; Navarrete et al., 2015). Deposition of these sediments resulted from an Atlantic marine transgression combined with regional tilting that have been linked to the Andean uplift (Haq et al., 1987; Nullo and Combina, 2011) and/or dynamic subsidence focused at the edges of a flat-slab segment (Gianni et al., 2018). Subsequent regression is recorded by the continental Río Chico Group (upper Paleocene – middle Eocene), which is deposited conformably above the Salamanca Formation (Feruglio, 1949; Krause and Bellosi, 2006; Raigemborn et al., 2010; Foix et al., 2013; Navarrete et al., 2015; Gianni et al., 2017). The Río Chico Group is characterized by alternating conglomerates, sandstones, clays and tuffs deposited in diverse fluvial environments (Foix et al., 2013 and references therein). The Río Chico Group evolves upwards to the middle Eocene – lower Miocene continental Sarmiento Formation, which is primarily composed of tuffaceous deposits that accumulated under low subsidence rates (Feruglio, 1949; Legarreta and Uliana, 1994; Figari et al., 1999, 2002; Bellosi, 2010; Ré et al., 2010; Dunn et al., 2013). The upper section of the Sarmiento Formation in central Patagonia is laterally interfingered with lower – middle Miocene marine deposits (Bellosi et al., 2002; Bellosi, 2010; Barreda and Bellosi, 2014; Paredes et al., 2015). Several marine transgressions from the Atlantic Ocean flooded most of the foreland and reached the present Andean piedmont during the Miocene (Ramos, 1982; Malumian and Nanez, 2011; Bechis et al., 2014; Encinas et al., 2018, 2019; Parras and Cuitiño, 2021). The resulting marine deposits are grouped into different units, all dated with $^{87}\text{Sr}/^{86}\text{Sr}$ chronostratigraphy on calcitic shells; they include: (i) the Chenque Formation in the San Jorge Basin assigned to 19.6 to 15.3 Ma (Cuitiño et al., 2015b) and limited to the west by the San

Bernardo FTB; (ii) the lower Miocene Monte León Formation (22.12 – 17.91 Ma) which surrounds the Deseado Massif (Parras et al., 2012); and (iii) the Centinela, Guadal, and El Chacay Formations (~19 Ma; Cuitiño et al., 2015a) which represent the westernmost deposits linked to Atlantic transgressions. These marine deposits grade transitionally to lower–middle Miocene fluvial and aeolian deposits of the synorogenic Santa Cruz Formation toward the east (Lesta et al., 1980; Barreda and Bellosi, 2014; Cuitiño et al., 2015a, 2016), and its western equivalents along the Cordillera known as the Río Zeballos Group (divided into the Río Jeinemeni, Cerro Boleadoras, and Río Correntoso formations). Pinturas Formation, Río Frías Formation and Galera Formation (Bown and Larriestra, 1990; Escosteguy et al., 2002; Escosteguy et al., 2003; Suárez et al., 2007; De la Cruz and Cortés, 2011; Perkins et al., 2012; Cuitiño et al., 2019). The age of the Santa Cruz Formation has been constrained to between 14 and 19 Ma by U–Pb zircon dating on intercalated tuffs (Blisniuk et al., 2005; Cuitiño et al., 2016; Cuitiño et al., 2021), while the equivalents Pinturas Formation and Galera Formation have been dated at 19–14 Ma (Perkins et al., 2012), and 18–12 Ma (Ray, 1996; Folguera et al., 2018), respectively. The Río Zeballos Group is poorly dated but a few studies indicate lower to middle Miocene ages (e.g., Espinoza et al., 2010). Only middle Miocene age have been obtained for the Río Frías Formation (Encinas et al., 2016). These sedimentary successions are enclosed by the middle Miocene to Pleistocene fluvio-glacial and alluvial units as the Río Mayo Formation dated at 13.4–11.8 Ma with the $^{40}\text{Ar}/^{39}\text{Ar}$ method (Dal Molin and Franchi, 1996; De Iuliis et al., 2008), and probably equivalent to the upper layers of the Santa Cruz Formation into the distal foreland. The deposition of these Cenozoic sediments into the foreland was coeval with several arc and within-plate volcanic episodes during the late Paleogene and the entire Neogene (Figure 3; Bruni et al., 2008; Gianni et al., 2015a; Suárez et al., 2015; Butler et al., 2020).

3 Materials and methods

Twenty samples were collected from Cenozoic sedimentary outcrops in the Cordillera, and the proximal and distal foreland (Table 1; Figure 2). Sedimentary rocks were collected from the Sarmiento (Figure 4A), San José (Figure 4B), Chenque (and equivalents; Figures 5A–5E), Santa Cruz (and equivalents; Figures 6A–6C) and Río Mayo Formations (Figures 7A–7B); providing an opportunity to investigate the evolution of the chain during a ~30 m.y. period from the late Eocene to the middle Miocene (Figure 3). In addition, AFT data from four Cretaceous samples collected in the southern San Bernardo FTB (MG7, MG9, MG17 and MG20; Figures 8A–8B) are also included in this study (Genge et al., 2021a).

All detrital samples were processed to extract apatite and zircon by standard mineral separation techniques including crushing, magnetic separation and heavy liquids (sodium polytungstate and methylene iodide with a density of 2.98 and 3.3 g/mL, respectively). AFT thermochronology was applied to all detrital samples whereas apatite U–Pb geochronology was limited to five samples selected from different sedimentary formations (four Cenozoic samples and one Cretaceous sample). Thirteen samples from a diverse set of formations ranging in age from the Cretaceous to the upper Miocene yielded a sufficient number of zircon crystals suitable for zircon in-situ U–Pb geochronology.

3.1 Zircon U–Pb dating

The youngest population of detrital zircon in a sedimentary rock provides the maximum depositional age (MDA) of the rock. Thus, according to Cawood et al. (2012) and Gehrels (2014), sedimentary rocks in foreland basins show a large proportion of zircons derived from syn-sedimentary volcanic activity. In such settings, the age of the youngest zircon population,

or MDA, may approximate the time of sediment deposition. Accordingly, forearc and foreland deposits in Andean settings have been successfully dated by U–Pb zircon systematics derived from the youngest group of zircons (e.g., Fosdick et al., 2017; Buelow et al., 2018; Witt et al., 2019).

The San Jorge Basin records a long-lived sedimentation coeval with active arc and intraplate volcanism deposits since the late Early Cretaceous (Figure 3). In this context all sampled sedimentary rocks are rich in volcanic clasts (Figures 4C, 5F, 5G, 6D, 6E, 7C, 8C and 8D), thus allowing more precise estimations of their age of deposition. Zircons were mounted in epoxy resin, polished and imaged by backscatter electron imaging. The mounts were cleaned in ultra-pure MQ water before their introduction in the ablation cell of the laser system. U, Th and Pb isotopic analyses were conducted by laser ablation inductively coupled plasma mass spectrometry (LA-ICP-MS) at Geosciences Montpellier (University of Montpellier, AEITE-ISO regional facility of the OSU ORISM[®]) using a ThermoFinnigan Element XR mass spectrometer coupled to a Teledyne (Cetac) Analyte G2 Excimer laser. Analytical conditions are similar to those described in previous reports (e.g., Bruguier et al., 2017) and are only summarized below. For each spot, a pre-ablation step consisting of 5 pulses was conducted using a spot diameter larger than the spot used for the analyses. For the analyses, the spot size was 50µm, with a repetition rate of 5Hz and an energy density of 5.5 J/cm². Ablation experiments were conducted under ultrapure helium to enhance sensitivity and reduce U–Pb fractionation (Gunther and Heinrich, 1999). After the sample cell, the laser aerosol was subsequently mixed with pure nitrogen to further increase sensitivity, and the sample with He–N₂ aerosol was then mixed with Ar before entering the plasma source. The U–Pb analysis time was 1 min, of which the first 15 s were devoted to the blank signal and the remaining 45 s were used for ablation of the sample. The matrix matching material 91500 (Wiedenbeck et al., 1995) was used to calibrate the Pb/Pb and Pb/U ratios of the unknowns. Secondary

standards were analyzed and regularly used to check accuracy of the results. These include GJ1 (Jackson et al., 2004) and Plešovice (Sláma et al., 2008). Raw data were processed by the Glitter® software (Van Achterberg et al., 2001). Ages were calculated using the IsoplotR program (Vermeesch, 2018; Table 2).

3.2 Apatite Fission Tracks

All samples were dated by the external detector method at the University of Padua (Italy) using a Zeta calibration factor for Fish Canyon and Durango age standards (Gleadow, 1981; Hurford, 1990). Apatite grains extracted from the sedimentary samples were mounted in epoxy, polished and etched in a 5M HNO₃ solution at 20°C for 20s to reveal spontaneous fission tracks. Apatite mounts were then covered by a U-poor mica sheet that serves as the external detector and irradiated at the Radiation Center of Oregon State University with a nominal fluence of 9×10^{15} neutrons/cm². Induced tracks on the mica detectors appeared after etching in 40% HF at 20°C for 40 min. Ages were obtained after fission tracks counting ($\zeta = 346 \pm 12$ for the CN5 dosimeter glass) on an Olympus optical microscope (magnification x 1250) and statistical processing with the Trackkey software (Dunkl, 2002; Table 3). Only 16 to 100 grains per sample were analyzed due to the paucity of apatite in some rocks (Table 3).

3.3 Apatite U–Pb dating

Fifty-three apatite grains, also dated by AFT, from four Cenozoic samples (MG4, MG12, MG49 and MG54) and one Cretaceous sample (MG20) were analyzed at the University of Perugia (Italy) with a quadrupole based Thermo Fisher Scientific iCAP-Q ICP-MS coupled with a Teledyne / Photon Machine G2 excimer laser ablation system. Fission track mounts

used for AFT thermochronology analysis were prepared for U–Pb analysis. Due to the small size of the apatite crystals, only one spot 30 µm in diameter was ablated per crystal, except for a few larger grains for which two ablations were performed. Madagascar apatite crystals (Thomson et al., 2012) were used as the primary reference material, while McClure apatite grains (Schoene and Bowring, 2006) were used for quality control. Data were reduced using Iolite software (Paton et al., 2011) and VizualAge_UcomPbline Data Reduction Scheme (Chew et al., 2014). The latter is a modified version of VizualAge (Petrus and Kamber, 2012) which corrects for the presence of variable common Pb in the primary reference material. To correct for the presence of common Pb in the unknowns two different approaches were used. The first consists of plotting the data on a Tera–Wasserburg diagram and visually identifying linear arrays. An array defines one population of co-genetic apatite grains from a single source, with the lower intercept giving the age and the upper intercept giving the initial $^{207}\text{Pb}/^{206}\text{Pb}$ ratio common Pb composition. The second approach allows for single grain age calculation and consists of an iterative approach that guess the initial $^{207}\text{Pb}/^{206}\text{Pb}$ ratio and calculate the corresponding ^{207}Pb corrected age (Chew et al., 2011). Discordia ages were calculated using IsoplotR (Vermeesch, 2018).

4 Results

Based on thin section observation from each sample, the presence of phenocrystals (olivine, pyroxene, feldspar and quartz) and numerous volcanic clasts in all samples suggest a persistent volcanic input through time (Figures 4C, 5F, 5G, 6D, 6E, 7C, 8C and 8D). This is further supported by petrographic analyses that indicate connection through time with the volcanic arc and/or coeval intraplate volcanism (e.g., Bellosi, 2010; Foix et al., 2020; Olazábal et al., 2020). The presence of numerous plutonic lithic fragments in the Santa Cruz

and Río Mayo deposits is also directly related to the synorogenic character of these sedimentary formations (Figures 6D, 6E, 7C, 8C and 8D) (e.g., Barreda and Bellosi, 2014).

4.1 Zircon U–Pb data

It is important to note that the accuracy of the MDA constraint depends on a number of factors, which must be considered when interpreting MDAs. This include, for example, the assumption that the youngest zircon grains present in the rock have indeed been analyzed, the time interval between the last magmatic/volcanic event occurring in the source area(s) and the deposition, the velocity of the uplift in these areas and the time spent before erosion and transport of the sediments in the basin. Of the 260 dated zircon grains in this study, 116 were selected for the calculation of MDAs for samples from the various formations. For this study, we define the MDAs as the weighted average of dates from the youngest clusters of at least two or three analyses overlapping at 2σ uncertainty (Dickinson and Gehrels, 2009). The youngest clusters in this study are systematically represented by at least 4 grains and are distinct on the concordia, with few or no grain coincidentally overlapping within error. Thus, our results may be considered robust (Sharman and Malkowski, 2020); although we acknowledge that the number of analyses involved in the MDA calculation is small for some samples (4 to 17 grains per sample). Nevertheless, it is interesting to note that most of the maximum deposition ages show a good correlation with previous depositional ages determined through $^{87}\text{Sr}/^{86}\text{Sr}$ chronostratigraphy, or $^{40}\text{Ar}/^{39}\text{Ar}$ and U–Pb geochronology on volcanic ashes (Cuitiño et al., 2015b; Cuitiño et al., 2016; Encinas et al., 2019). Samples from the marine Chenque and equivalents (Figure 5), and continental Santa Cruz Formations (Figure 6) provide ages that are early Miocene (from 16.22 ± 0.60 to 20.78 ± 0.93 Ma and from 17.54 ± 0.47 to 17.83 ± 0.39 Ma respectively), which suggests simultaneous deposition

of these sedimentary formations across the foreland (Figures 5H–5K, 6E–6G). Similarly, one sample from the San José Formation (MG43) provides a MDA of 40.4 ± 0.4 Ma (MSWD = 0.3, n = 13), consistent with a previous age determination (Encinas et al., 2019). Lastly, the youngest analysis of the Cretaceous sample from the Chubut Group collected in the San Bernardo FTB yield an Albian MDA of 103.1 ± 0.5 Ma (MSWD = 0.12, n = 4; Figure 8E) which is also consistent with previous studies (Cuitiño et al., 2015b; Suárez et al., 2009). We thus consider the MDAs for these samples and locations to constitute a close approximation of the true depositional age. However, discrepancies are evident for other samples. For example, samples from the Río Mayo and Sarmiento Formations yield MDAs that are significantly older than the depositional ages estimated in previous works (Figure 9) (De Iuliis et al., 2008; Ré et al., 2010; Dunn et al., 2013) with an age difference reaching ca. 50 m.y. for the Sarmiento Formation. For these samples, the MDAs are best interpreted as the age of one of the source components feeding detritus to the basin.

All the data used to obtain the MDAs on the sedimentary series are reported in Table 2 with uncertainties reported at the 2σ level. Detrital U–Pb zircon results are also shown as concordia diagrams (Figures 4D–F, 5H–I, 6E–G, 7D–E and 8E) and as a Kernel density plot, generated using IsoplotR (Vermeesch, 2018). The density plot allows us to define three main volcanic phases during (1) the Miocene, (2) the late Paleogene, and (3) the Cretaceous (Figure 9).

4.2 AFT data

Despite the low closure temperature of the AFT thermochronometer (~ 110 °C; e.g., Ketcham et al., 2007), the comparison of single-grain ages with depositional ages in radial plots indicates that the Cenozoic samples were never fully reset (Figure 10), and thus were not subjected to any substantial post-depositional heating. Given the small amount of subsidence

thought to occur during the Cenozoic, these data can be interpreted as the time of exhumation of the sediment sources.

Analyses were subjected to a χ^2 test in order to identify any statistical scattering of single-grain dates and to detect the presence of multiple age components. For samples which did not pass the test ($\chi^2 < 5$), grain-age distributions were decomposed with IsoplotR finite mixture modeling (Vermeesch, 2018). The AFT ages in Cenozoic deposits vary widely (from ~20 Ma to ~180 Ma) but can be grouped into four distinct populations. Most of the Miocene samples show an age component (here named P1) that ranges from approximately 20 to 40 Ma (Table 3). A second age component (P2) corresponds to Paleocene–middle Eocene ages (ca. from 40 to 60 Ma). Surprisingly, most of the Miocene samples, as well as the sample from the San José Formation, show a single population corresponding to either P1 or P2 components, as indicated by a chi-squared probability $P(\chi^2) > 5\%$. Only three samples exhibit both P1 and P2 components: MG12, MG48 and MG49. For sample MG54, in addition to the P1 component, an older component with Late Cretaceous ages (P3) has been detected. These Cretaceous ages have also been identified in the three middle Eocene – lower Miocene samples from the Sarmiento Formation. The oldest component (P4) yields Jurassic ages and has been detected in only two samples from the Sarmiento Formation (MG1 and MG3), collected directly south of the San Bernardo FTB.

To help interpret the data and add some additional constraints, the detrital AFT data combined with AFT data from the Cretaceous deposits of the San Bernardo FTB (Genge et al., 2021a), have been analyzed using a multi-dimensional scaling (MDS) method. This is a dimension-reducing technique that objectively analyzes the level of similarity of individual data (Borg and Groenen, 2005) and has been adapted for use in provenance studies (Vermeesch, 2013). The method is based on pairwise dissimilarities between samples translated onto a scatter plot in which similar samples plot close together (Vermeesch et al., 2016), and has been shown to

be efficient for comparing samples in complex detrital dataset. Here we choose a distributional dataset including single-grain AFT data and related analytical uncertainties with the Sircombe-Hazelton distance. The results indicate two distinct groups characterized by short distances between the samples (Figure 11A): (1) Miocene deposits and San José Formation rocks; and (2) Sarmiento Formation rocks with Cretaceous deposits. This result is fully consistent with the AFT populations identified by binomial peak-fitting algorithm on IsoplotR (Vermeesch, 2018). The corresponding 'Shepard plot' (Figure 11B) displaying a linear array and a low stress value (< 0.15), illustrating the good fit of our data in this non-metric configuration.

4.3 Apatite U–Pb data

When dating apatite by the U–Pb method, large uncertainties can be obtained as a result of low U and correspondingly low radiogenic Pb content often occurring in young grains. Of the apatite grains with AFT analyses 53 grains from 5 different samples have also been dated with U–Pb (Table 4; Supplementary Material Figure S1). Of these, 36 grains produced large age uncertainties, i.e. 2σ errors > 25% (as in Zattin et al., 2012; Mark et al., 2016), or yield ages with negative values. However, we identified 17 grains that provide robust age results, with individual corrected ages (following the iterative approach of Chew et al., 2011) ranging from 84.6 ± 28.5 Ma to 159.9 ± 75.7 Ma (Table 4). Plotted in the Tera–Wasserburg diagram (red circles and trend in Figure 12A; Figures 12B–E), these grains from each sample form a linear trend systematically giving a Cretaceous age for the lower intercept, i.e., ranging from 94.9 ± 28.6 Ma to 119.0 ± 16.6 Ma, and a value ranging from 0.83 to 0.85 for the $^{207}\text{Pb}/^{206}\text{Pb}$ axis intercept. The “Cretaceous” population, clearly present in three of the Miocene samples (Figures 12C–12E), is thus considered meaningful and related to the age of the source

material. This is also consistent with the numerous Cretaceous ages obtained on zircon crystals (population 3 in Figure 9).

The linear arrays obtained with the other 36 grains (i.e., 2σ errors $> 25\%$, negative age values) yield more questionable ages (blue circles and trend in Figure 12A, Figures 12C–E). Nevertheless, they suggest the existence of a younger population in the Miocene samples (Figures 12C–12E) with ages similar to the AFT P1 component and the zircon U–Pb ages (population 1 in Figure 9). Thus, this younger population is most likely related to a syn-sedimentary volcanic input. The difference in the ages obtained from U–Pb apatite and zircon dating may be simply explained by the small number of grains dated, resulting in large errors and some negative values for many grains. Nevertheless, a Cretaceous population as well as a younger population (probably syn-depositional) are recognized in both the apatite and zircon data.

5 Discussion

The results of the detrital AFT dating define four main populations (Table 3; Figure 10) belonging to two groups of samples, as evidenced by the MDS results: (1) the samples characterized by the presence of P1 and P2 components, i.e. Miocene deposits (Chenque and equivalents, Santa Cruz and Río Mayo Formations) and the sample from the Eocene San José Formation; and (2) the samples displaying systematically older P3 and P4 components, i.e. the deposits from the middle Eocene – lower Miocene Sarmiento Formation, collected along the southern and eastern margin of the San Bernardo FTB. As for the U–Pb dating, both the apatite and zircon, results identify two populations in the Cenozoic samples, with presumed syn-depositional U–Pb ages and Cretaceous U–Pb ages, as well as a late Eocene–early Oligocene population recognized only with zircon U–Pb dating (Figures 9 and 12A). The

Cordillera and the intraplate belt share a similar geochronological signal (Paleozoic–Triassic basement, magmatic and volcaniclastic rocks during the Cretaceous and the Cenozoic; Figure 2), while having contrasting thermal histories (Figure 1). Thus, the detrital signal evidenced by the U–Pb analyses (Figure 9 and 12) may not be as useful for identifying the source location as the AFT data.

5.1 Provenance during the Eocene-early Miocene in the north-eastern San Jorge Basin

Cretaceous AFT ages (population P3) have been detected along the southern and eastern margin of the San Bernardo FTB (Figure 13A) in the middle Eocene–lower Miocene continental samples from the Sarmiento Formation (MG1, MG3 and MG55) and in one sample from the Miocene deposits (MG54). The samples from the Sarmiento Formation are most likely of the middle Eocene–Oligocene ages as early Miocene ages have only been recognized in few localities (Ré et al., 2010; Dunn et al., 2013). Furthermore, the MDAs obtained for the Sarmiento Formation clearly indicate a significant source of Cretaceous age material (Figure 9). This suggests that some of the sediments that compose the Sarmiento Formation may be derived from the erosion of (i) the Chubut Group exposed along the adjacent intraplate San Bernardo FTB (Figure 13A) (Genge et al., 2021a), or (ii) the volcanic Divisadero Group along the Andes (Figure 2) (e.g., Suárez et al., 2009; Suárez et al., 2014). Despite the consistent results obtained for the Sarmiento deposits, the contemporary San José Formation (sample MG43), located into the present Cordillera, yields a non-reset AFT P1 component (20–40 Ma) and an Eocene MDA (~40 Ma) that could be related to a major syn-depositional volcanic arc input. The latter sample also appears together with Miocene deposits in the MDS diagram, while the Sarmiento Formation deposits have a provenance signature similar to the samples from the Cretaceous Chubut Group collected from the San Bernardo

FTB (Genge et al., 2021a). Furthermore, the existence of the oldest component P4 in two samples of the Sarmiento Formation (MG1 and MG3) is consistent with sourcing from the Chubut Group exposed along the San Bernardo FTB. Indeed, despite the large error for the P4 component in the sample MG1, these ages may be attributed to Jurassic clasts from underlying formations that are occasionally recognized in the deposits of the Chubut Group (Foix et al., 2020). We therefore suggest that the occurrence of the Mesozoic P3 and P4 components, as well as the observed differences between Sarmiento and San José deposits (e.g., MDA, MDS), testify to the exposure of the San Bernardo FTB during the deposition of the Sarmiento Formation. The reappearance of Cretaceous AFT ages in one Miocene rock (MG54) may indicate drainage reorganization with the Sarmiento Formation and/or a direct source of Cretaceous units exposed along the San Bernardo FTB (Figure 13B).

5.2 Volcanic content in Miocene deposits

In detrital thermochronology studies, the youngest cooling age population (here P1) is usually paired with the sedimentation age to measure the lag time in order to obtain information on the exhumation history of the source rock, assuming that the age of grains is not related to volcanic input (Garver et al., 1999; Bernet et al., 2001). Indeed, along the Andes, the exhumation signal may be easily overtaken by the volcanic input, which is evident from the presence of considerable pyroclasts throughout the entire region (Figure 3). Therefore, the combined application of U–Pb and AFT analysis on the same apatite crystals is useful for discriminating the presence of syn-depositional volcanic apatite. In the case of volcanism, the single-grain U–Pb and AFT ages obtained should be very similar to the depositional age as cooling is almost instantaneous.

A significant volcanic input can be recognized in all the samples by the presence of various phenocrystals and numerous volcanic clasts observed in the thin sections (Figures 4C, 5F, 5G, 6D, 6E, 7C, 8C and 8D). Our results from double dating confirm a volcanic input in Miocene sedimentary strata (i.e., apatite U–Pb ages overlap within error of the P1 component; Figure 12) and Cretaceous deposits (i.e., apatite U–Pb ages overlap within error with the AFT ages of Genge et al., 2021a; Figure 12B). This Miocene volcanic input is consistent with literature that describes volcanic activity through the Neogene (Suárez et al., 2015; Butler et al., 2020). Thus, the abundance of volcanic apatite in our samples impedes the use of lag time concept in this study in order to quantify exhumation rates (see lag time diagram obtained in Supplementary material, Figure S2).

5.3 Provenance of Miocene deposits

In addition to assessing syn-depositional volcanism, double dating of apatite in Cenozoic deposits allows us to identify source rocks crystallized between 120 and 90 Ma, and were then exhumed during the Cenozoic (20–40 Ma). However, an identification of the source area is extremely difficult as all the data are remarkably uniform. Therefore, the uniformity of the detrital AFT thermochronology results across the foreland (Figure 13A), the consistency of U–Pb apatite and zircon ages (Figures 9 and 12), and the results obtained from MDS statistics (Figure 11A) all suggest a similar source of Miocene deposits across the entire study area, despite the changes in sedimentation style and depositional environments through time.

Remarkably, detrital AFT ages belonging to the P1 population (20–40 Ma) are coincident with granitoid ages obtained in the western and eastern Patagonian Cordillera (Figure 1; Thomson et al., 2001, 2010), whereas much older AFT ages have been recognized in bedrocks of the Deseado Massif (Fernández et al., 2020; Derycke, 2021), in Cretaceous

sedimentary rocks of the San Bernardo FTB (Genge et al., 2021a), and in Paleogene sedimentary rocks surrounding the San Bernardo FTB (this study). Our data therefore point to the Cordillera as a primary contributor of sediments for the San Jorge Basin during the early Miocene, a result consistent with paleoflow indicators (e.g., Guillaume et al., 2009).

Although less well represented but nevertheless widespread, the component P2 (40–60 Ma) suggests an active source exhuming during the Paleocene–middle Eocene, given that the U–Pb zircon ages likely indicate no significant coeval volcanic activity during this period (Figure 9). The P2 component is not recorded in the sandstones of the Santa Cruz Formation (~47°S) but is present in the two samples of the Río Mayo Formation (~46°S), collected in the Río Mayo sub-basin, in three samples from the Monte León formation south and east of the Deseado Massif (~48°S), and in one sample from the Ichique formation in the distal San Jorge Basin (Figure 13A). The Río Mayo sub-basin is bordered to the west by the Cretaceous Patagonian Batholith for which few Paleocene–middle Eocene and late Eocene – early Miocene bedrock AFT cooling ages have been proposed (Figure 1) (Thomson et al., 2010). A direct connection between a western source and the Río Mayo sub-basin can be therefore inferred (Figure 13C). This sector of the Cordillera probably represented a major source for the Río Mayo sub-basin, however, recycling of the surrounding Paleocene–middle Eocene volcanic deposits cannot be excluded. For the sediments that were deposited close to the present-day Atlantic coast during the Miocene, the distribution of detrital AFT data (Figure 13A) and the drainage reconstructions proposed by Guillaume et al. (2009) may also suggest a Cordillera source. However, one Miocene sample (MG54) containing Cretaceous AFT ages (P3 component) may indicate minor recycling of the Chubut Group or Sarmiento Formation deposits in this area.

A recent thermochronology study in the Deseado Massif defined a few Paleocene–middle Eocene AFT ages (Fernández et al., 2020), suggesting that the Deseado Massif is, indeed, a

potential source for the P2 component in the surrounding areas as identified in samples MG47, MG48 and MG49. However, detrital data obtained from around the Deseado Massif do not show the Cretaceous AFT ages that are dominant in the bedrock analysis (Fernández et al., 2020; Derycke, 2021). Therefore, despite its proximity with the surrounding basins and the presence of the P2 component in samples collected south of the Deseado Massif, we infer that this intraplate belt was not actively eroding during the Miocene (Figure 13C), although it did represent a significant source during the Late Cretaceous (Limarino and Giordano, 2016). Thus, the P2 component observed south of the Deseado Massif may also derive from the Cordillera.

To summarize, the AFT results support the idea of a direct sediment route from the magmatic arc to the distal foreland through the early and middle Miocene.

5.4 Patagonian reliefs denudation vs recycling through the Cenozoic

The first shortening event in the Patagonian Andes started during the late Early Cretaceous and persisted to the middle Eocene. This phase has been evidenced by angular unconformities recognized between Aptian and Albian deposits (Giacosa et al., 2010), growth-strata observed in coeval Upper Cretaceous and Paleogene deposits (Navarrete et al., 2016; Gianni et al., 2017), and thermochronological data (Savignano et al., 2016; Genge et al., 2021b; among others) both along the Cordillera and in the broken foreland. This deformation period is followed by a neutral tectonic regime across the retroarc region (Horton et al., 2016; Horton and Fuentes, 2016) coeval with a regional subsidence reported from the late Eocene to the middle Miocene through the entire Patagonian foreland (Bechis et al., 2014; Echaurren et al., 2016; Fernández Paz et al., 2018, 2020). This regional subsidence is ascribed to a long-term slab roll-back and a particularly low trench-normal absolute velocity since the middle Eocene

(Figure 3) (Muñoz, 1999; Ramos and Folguera, 2005; Orts et al., 2012; Maloney et al., 2013).

During times of relative tectonic quiescence, drainage and eustatic sea-level changes may govern sediment deposition. Thus, as subsidence was prevalent in the central Patagonian foreland and Cordillera during this period, the resulting marine floods occurred over a large area (e.g., Bechis et al., 2014; Encinas et al., 2018).

The intraplate belt of central Patagonia (Deseado Massif and San Bernardo FTB) may have represented positive reliefs preventing the deposition of Miocene marine sediments far into these areas (e.g., Encinas et al., 2018). Nevertheless, the lack of Cretaceous AFT ages in Miocene samples indicates that the intraplate belt was not a major source of sediments during the Miocene, probably due to the absence of any significant erosion. However, these reliefs may have represented a major sediment source for surrounding areas from the Late Cretaceous (Deseado Massif; Limarino and Giordano, 2016) until the early Miocene (San Bernardo FTB; this study). This inferred decrease in erosion processes which may be related to 1) climate evolution, 2) eustatic sea-level changes, or 3) post-orogenic erosional processes. Constant extratropical and highly seasonal climate characterized the central Patagonia during the late Eocene through the end of the early Miocene, when an increase in aridity is observed (Blisniuk et al., 2005; Palazzi et al., 2014; Kohn et al., 2015). As a stable climate has been inferred for this area during the deposition of the Sarmiento Formation, the change in erosion behavior during the Miocene is probably not related to climatic evolution. Sea-level fluctuations most likely affected coastal areas and thus may not have a significant impact on the erosion of the San Bernardo FTB (Ethridge et al. 1998). The most plausible hypothesis may be related to post-orogenic erosional processes. Indeed, due to a tectonic quiescence after their formation during the Early Cretaceous–middle Eocene, the intraplate belt experienced a decrease in erosion, as inferred from provenance inputs derived from our data.

Whereas the erosion decreased significantly at the San Bernardo FTB during the early Miocene, the denudation of the Cordillera seems to have continued through time. Indeed, deep and shallow marine deposits have also been identified with fossil records indicating Pacific and Atlantic origins along the western and the eastern areas of the Patagonian Cordillera, respectively (Encinas et al., 2018). Although these deposits are geographically close, the lack of an extended transient connection between the Pacific and the Atlantic in the Patagonian Andes suggests the persistence of existing topographic relief acting as an orographic barrier during marine incursion from the late Paleogene to early Neogene (Ramos, 1982; Mpodozis and Ramos, 1990; Frassinetti and Covacevich, 1999). Furthermore, a few AFT ages in the central Patagonian Cordillera show that this region was governed by denudation processes at ca. 30 Ma (Figure 1) (Thompson et al., 2001; 2010). This result is also consistent with data from the eastern front adjacent to the Neuquén and the Magallanes retroarc basin, which are north and south of the current study area, respectively (e.g., Bande et al., 2012; Folguera et al., 2015; Leonard et al., 2020).

Nevertheless, this singularly consistent signature over a large area and through the Miocene may indicate extensive mixing of sediments derived from recycling of exposed sedimentary successions. The detrital AFT components clearly indicate that, at least around the San Bernardo FTB, there was very limited recycling of the overlying Sarmiento Formation during the deposition of the marine Chenque Formation (and equivalents). Then, the deposition of the Santa Cruz Formation occurred during the middle Miocene Andean phase and is related to an excess sediment supply, resulting from the moderate and steady creation of accommodation space (Nullo and Combina, 2002; Cuitiño et al., 2021). Previous works in surrounding areas also recognized sediment recycling processes during the deposition of the Santa Cruz Formation (e.g., Fosdick et al., 2015). The consistency of results obtained in this study for the Santa Cruz Formation may be mostly related to the erosion of the Cordillera

during the Miocene shortening phase, although moderate impacts from recycling processes cannot be totally excluded. The MDAs from the Río Mayo Formation that were found to be older than expected (Figure 9) are coherent with major recycling processes. This is consistent with the results of Folguera et al. (2018), who attributed them to the recycling of previous syn-orogenic detrital components in the eastern Andean front during the middle Miocene. Therefore, results indicate that grains identified into the Miocene foreland successions were derived both from the Cretaceous Patagonian magmatic arc exposed along the entire Cordillera (Figure 2) and from recycling processes. Our data also suggest that no significant sediment source from the intraplate belts was active during the Miocene.

6 Conclusions

Detrital thermochronology in the central Patagonian foreland basin is dominated by a persistent volcanic signal during the Miocene. Nevertheless, it provides valuable provenance information on source denudation history. Our findings highlight that:

- (1) the San Bernardo FTB was an active sediment source from late Eocene to early Miocene times;
- (2) the Deseado Massif and the San Bernardo FTB were stable during the early–middle Miocene period as supported by the waning of sediment contribution from these areas in marine and continental Miocene deposits, the latter being deposited during the Miocene Andean orogenic phase;
- (3) the adjacent Cordillera was the primary source of sediments for the proximal and distal foreland during Miocene times;

- (4) recycling processes seem to be secondary, apart from middle Miocene sediments deposited along the eastern Andean front;
- (5) the denudation phase along both the Cordillera and broken foreland started after the cessation of the significant shortening episode that affected the entire area in the late Early Cretaceous–middle Eocene. Thus, the central Patagonian topographic relief were governed by post-orogenic erosional processes within a general context of a regional subsidence, and contributed variously to sedimentation into adjacent subsiding foreland troughs.

Acknowledgements

Funding for this work was provided by the University of Padova (Progetto di Ateneo 2015, CPDA158355) and the INSU (Institut National des Sciences de l'Univers, France) through a Telus-Syster scholarship. S. Boesso and V. di Tauro are thanked for sample preparation. We thank Valerio Olivetti for helpful discussions that helped to construct this manuscript.

References

- Actherbergh, E., 2001. Data reduction software for LA-ICP-MS. Laser Ablation-ICP-mass spectrometry in the earth sciences: principles and applications, 239-243.
- Adriasola, A.C., Thomson, S.N., Brix, M.R., Hervé, F., Stöckhert, B., 2006. Postmagmatic cooling and late Cenozoic denudation of the North Patagonian Batholith in the Los Lagos region of Chile, 41°-42°15' S. International Journal of Earth Sciences 95, 504–528.
- Allard, J.O., Foix, N., Bueti, S.A., Sánchez, F.M., Ferreira, M.L., Atencio, M., 2020. Comparative structural analysis of inverted structures in the San Bernardo fold belt (Golfo

San Jorge basin, Argentina): Inversion controls and tecto-sedimentary context of the Chubut Group. *Journal of South American Earth Sciences* 97, 102405.

Anselmi, G., Panza, J.L.A., Cortés, J.M., Ragona, D., 2004. Hoja Geológica 4569-II El Sombrero. Servicio Geológico Minero Argentino. Instituto de Geología y Recursos Minerales.

Aramendía, I., Cuitiño, J. I., Ghiglione, M., & Bouza, P. J. (2019). Tectonostratigraphic significance of the Neogene sedimentary record of northwestern Austral-Magallanes basin, Argentinean Patagonia. *Latin American journal of sedimentology and basin analysis*, 26(2), 99-126.

Ardolino, A.A., Panza, J.L.A., Ylláñez, E.D., Parisi, C., Franchi, M., 2003. Hoja Geológica 4566-I Garayalde. Servicio Geológico Minero Argentino. Instituto de Geología y Recursos Minerales.

Bande, A., Horton, B.K., Ramírez, J.C., Mora, A., Parra, M., Stockli, D.F., 2012. Clastic deposition, provenance, and sequence of Andean thrusting in the frontal Eastern Cordillera and Llanos foreland basin of Colombia. *Bulletin* 124, 59–76.

Barreda, V., Bellosi, E., 2014. Ecosistemas terrestres del Mioceno Temprano de la Patagonia central, Argentina: primeros avances. *Revista del Museo Argentino de Ciencias Naturales nuevas serie* 5, 125–134.

Bechis, F., Encinas, A., Concheyro, A., Litvak, V.D., Aguirre-Urreta, B., Ramos, V.A., 2014. New age constraints for the Cenozoic marine transgressions of northwestern Patagonia, Argentina (41–43° S): Paleogeographic and tectonic implications. *Journal of South American Earth Sciences* 52, 72–93.

Bellosi, E., Palamarczuk, S., Barreda, V., Sanagua, J., Jalfin, G., Herbst, R., 2000. Litofacies y palinología del contacto Grupo Chubut-Formación Salamanca en el

oeste de la cuenca del Golfo San Jorge, in: 11 Simposio Argentino de Paleobotánica y Palinología.

Bellosi, E.S., 2010. Loessic and fluvial sedimentation in Sarmiento Formation pyroclastics, middle Cenozoic of central Patagonia. The Paleontology of Gran Barranca: Evolution and Environmental Change through the Middle Cenozoic of Patagonia. Cambridge University Press, Cambridge 278–292.

Bellosi, E.S., Miquel, S.E., Kay, R.F., Madden, R.H., 2002. Un paleosuelo mustersense con microgastrópodos terrestres (Charopidae) de la Formación Sarmiento, Eoceno de Patagonia central: significado paleoclimático. *Ameghiniana* 39, 465–477.

Bernet, M., Zattin, M., Garver, J.I., Brandon, M.T., Vance, J.A., 2001. Steady-state exhumation of the European Alps. *Geology* 29, 35–38.

Blisniuk, P. M., Stern, L. A., Chamberlain, C. P., Idleman, B., & Zeitler, P. K., 2005. Climatic and ecologic changes during Miocene surface uplift in the Southern Patagonian Andes. *Earth and Planetary Science Letters*, 230(1-2), 125-142.

Borg, I., Groenen, P.J., 2005. Modern multidimensional scaling: Theory and applications. Springer Science + Business Media.

Bosch, D., Garrido, C. I., Bruguier, O., Dhuime, B., Bodinier, J. L., Padrón-Navarta, J. A., & Galland, B., 2011. Building an island-arc crustal section: time constraints from a LA-ICP-MS zircon study. *Earth and Planetary Science Letters*, 309(3-4), 268-279.

Bown, T. M., & Larriestra, C. N. (1990). Sedimentary paleoenvironments of fossil platyrhine localities, Miocene Pinturas Formation, Santa Cruz Province, Argentina. In *The Platyrhine Fossil Record* (pp. 87-119). Academic Press.

Breitsprecher, K., Thorkelson, D.J., 2009. Neogene kinematic history of Nazca–Antarctic–Phoenix slab windows beneath Patagonia and the Antarctic Peninsula. *Tectonophysics* 464, 10–20.

Bridge, J. S., Jalfin, G. A., & Georgieff, S. M., 2000. Geometry, lithofacies, and spatial distribution of Cretaceous fluvial sandstone bodies, San Jorge Basin, Argentina: outcrop analog for the hydrocarbon-bearing Chubut Group. *Journal of Sedimentary Research*, 70(2), 341-359.

Bruguier, O., Bosch, D., Caby, R., Vitale-Brovarone, A., Fernandez, L., Hammor, D., Laouar, R., Ouabadi, A., Abdallah, N. and Mechati, M. 2017. Age of UHP metamorphism in the Western Mediterranean: Insight from rutile and zircon inclusions in a diamond-bearing garnet megacryst (Edough Massif, NE Algeria). *Earth and Planetary Science Letters*, 474, 215-225

Bruni, S., d'Orazio, M., Haller, M.J., Innocenti, F., Manetti, P., Pecskay, Z., Tonarini, S., 2008. Time-evolution of magma sources in a continental back-arc setting: the Cenozoic basalts from Sierra de San Benito (Patagonia, Chubut, Argentina). *Geological Magazine* 145, 714–732.

Buelow, E. K., Suriano, J., Maroney, J. B., Kimbrough, D. L., Mescua, J. F., Giambiagi, L. B., & Hoke, G. D. (2018). Sedimentologic and stratigraphic evolution of the Cacheuta basin: Constraints on the development of the Miocene retroarc foreland basin, south-central Andes. *Lithosphere*, 10(3), 366-391.

Butler, K.L., Herton, B.K., Echaurren, A., Folguera, A., Fuentes, F., 2020. Cretaceous-Cenozoic growth of the Patagonian broken foreland basin, Argentina: Chronostratigraphic framework and provenance variations during transitions in Andean subduction dynamics. *Journal of South American Earth Sciences* 97, 102242.

Cande, S.C., Leslie, R.B., 1986. Late Cenozoic tectonics of the southern Chile trench. *Journal of Geophysical Research: Solid Earth* 91, 471–496.

Carrapa, B., DeCelles, P.G., Reiners, P.W., Gehrels, G.E., Sudo, M., 2009. Apatite triple dating and white mica $^{40}\text{Ar}/^{39}\text{Ar}$ thermochronology of syntectonic

detritus in the Central Andes: A multiphase tectonothermal history. *Geology* 37, 407–410.

Cawood, P. A., Hawkesworth, C. J., & Dhuime, B. (2012). Detrital zircon record and tectonic setting. *Geology*, 40(10), 875-878.

Cherniak, D.J., Lanford, W.A., Ryerson, F.J., 1991. Lead diffusion in apatite and zircon using ion implantation and Rutherford backscattering techniques. *Geochimica et Cosmochimica Acta* 55, 1663–1673.

Chew, D.M., Petrus, J.A., Kamber, B.S., 2014. U–Pb LA–ICPMS dating using accessory mineral standards with variable common Pb. *Chemical Geology* 363, 185–199.

Chew, D.M., Sylvester, P.J., Tubrett, M.N., 2011. U– ^{238}Pb and Th–Pb dating of apatite by LA-ICPMS. *Chemical Geology* 280, 200–216.

Clavijo, R., 1986. Estratigrafía del Cretácico Inferior en el sector occidental de la Cuenca del Golfo San Jorge. *Boletín de Informaciones Petroleras* 9, 15–32.

Clyde, W.C., Wilf, P., Iglesias, A., Slingerland, R.L., Barnum, T., Bijl, P.K., Bralower, T.J., Brinkhuis, H., Comer, F.E., Huber, B.T., 2014. New age constraints for the Salamanca Formation and lower Río Chico Group in the western San Jorge Basin, Patagonia, Argentina: Implications for Cretaceous-Paleogene extinction recovery and land mammal age correlations. *Bulletin* 126, 282–306.

Cobos, J.C., Parza, J.L.A., Zubía, M.A., Figari, E.G., Cardinali, G., Lucero, M., Borderas, M., 2003. Hoja Geológica 4769-I El Pluma. Servicio Geológico Minero Argentino. Instituto de Geología y Recursos Minerales.

Cortiñas, J.S., 1996. La cuenca de Somuncurá-Cañadón Asfalto: sus límites, ciclos evolutivos del relleno sedimentario y posibilidades exploratorias, in: XIII Congreso Geológico Argentino y III Congreso de Exploración de Hidrocarburos, Buenos Aires, Actas. pp. 147–163.

U–PbCuitiño, J.I., Santos, R.V., Muruaga, P.J.A., Scasso, R.A., 2015a. Sr-stratigraphy and sedimentary evolution of early Miocene marine foreland deposits in the northern Austral (Magallanes) Basin, Argentina. *Andean Geology* 42, 364–385.

Cuitiño, J.I., Scasso, R.A., Santos, R.V., Mancini, L.H., 2015b. Sr ages for the Chenque Formation in the Comodoro Rivadavia región (Golfo San Jorge basin, Argentina): stratigraphic implications. *Latin American journal of sedimentology and basin analysis* 22, 3–12.

Cuitiño, J. I., Fernicola, J. C., Kohn, M. J., Trayler, R., Neipauer, M., Bargo, M. S., Kay R. F., Vizcaíno, S. F., 2016. U–Pb geochronology of the Santa Cruz Formation (early Miocene) at the Río Bote and Río Santa Cruz (southernmost Patagonia, Argentina): Implications for the correlation of fossil vertebrate localities. *Journal of South American Earth Sciences*, 70, 103–110.

Cuitiño, J.I., S.F Vizcaíno, M.S. Bargo and I. Aramendía, 2019. Sedimentology and fossil vertebrates of the Santa Cruz Formation (early Miocene) in Lago Posadas, southwestern Patagonia, Argentina. *Andean Geology*, 46:383-420.

Cuitiño, J. I., Sol Raiger, M., Susana Bargo, M., Vizcaíno, S. F., Muñoz, N. A., Kohn, M. J., & Kay, R. F. (2021). Insights on the controls on floodplain-dominated fluvial successions: a perspective from the Early–Middle Miocene Santa Cruz Formation in Río Chalía (Patagonia, Argentina). *Journal of the Geological Society*, 178(4), jgs2020-188.

Dal Molin, C.N., 1998. Hoja Geológica 4572-IV Alto Río Senguerr.

Dal Molin, C.N., Franchi, M., 1996. X111 Congreso Geológico Argentino y 111 Congreso de Exploración de Hidrocarburos, Actas 1.-4 73-4 78 Reinterpretacion estratigrafica de las sedimentitas terciarias del suroeste de Chubut, in: Congreso de Exploracion de Hidrocarburos. La Asociación, p. 473.

- De Iuliis, G., Kay, R., F Vizcaíno, S., 2008. Fossil mammals of the late Miocene (11.6–5.3 million years ago) Santa Cruz Formation (SCF), Santa Cruz (Patagonia), Argentina.
- de la Cruz, R., & Cortés, J. (2011). Geología del área oriental de la Hoja Puerto Cisnes, Región Aysén del Gral. Carlos Ibáñez del Campo. Serie Geología Básica, 127, 1-70.
- DeCelles, P.G., Giles, K.A., 1996. Foreland basin systems. *Basin research* 8, 105–123.
- DeCelles, P.G., Horton, B.K., 2003. Early to middle Tertiary foreland basin development and the history of Andean crustal shortening in Bolivia. *Geological Society of America Bulletin* 115, 58–77.
- Derycke, A., 2021. Évolution géodynamique du Massif du Deseado (Patagonie): apport d'une nouvelle approche multi-thermochronologique basse température (Doctoral dissertation, Université Paris-Saclay).
- Dickinson, W. R., & Gehrels, G. E. (2009). Use of U–Pb ages of detrital zircons to infer maximum depositional ages of strata: a test against a Colorado Plateau Mesozoic database. *Earth and Planetary Science Letters*, 288(1-2), 115-125.
- Dunkl, I., 2002. TRACKIT: a Windows program for calculation and graphical presentation of fission track data. *Computers & Geosciences* 28, 3–12.
- Dunn, R. E., Madden, R. H., Kohn, M. J., Schmitz, M. D., Strömberg, C. A., Carlini, A. A., Ré, G. H., & Crowley, J. (2013). A new chronology for middle Eocene–early Miocene South American land mammal ages. *Bulletin*, 125(3-4), 539-555.
- Echaurren, A., Folguera, A., Gianni, G., Orts, D., Tassara, A., Encinas, A., Giménez, M., Valencia, V., 2016. Tectonic evolution of the North Patagonian Andes (41–44 S) through recognition of syntectonic strata. *Tectonophysics* 677, 99–114.
- Echaurren, A., Oliveros, V., Folguera, A., Ibarra, F., Creixell, C., & Lucassen, F., 2017. Early Andean tectonomagmatic stages in north Patagonia: insights from field and geochemical data. *Journal of the Geological Society*, 174(3), 405-421.

Encinas, A., Pérez, F., Nielsen, S. N., Finger, K. L., Valencia, V., & Duhart, P., 2014. Geochronologic and paleontologic evidence for a Pacific–Atlantic connection during the late Oligocene–early Miocene in the Patagonian Andes (43–44° S). *Journal of South American Earth Sciences*, 55, 1–18.

Encinas, A., Folguera, A., Litvak, V. D., Echaurren, A., Gianni, G., Fernández Paz, F., Bobe, R., & Valencia, V. (2016). New age constraints for the Cenozoic deposits of the Patagonian Andes and the Sierra de San Bernardo between 43 and 46° S. In I Simposio de tectónica Sudamericana (Vol. 140).

Encinas, A., Folguera, A., Bechis, F., Finger, K.J., Zambrano, P., Pérez, F., Bernabé, P., Tapia, F., Riff, J., Molina, P., Paz, L.F., Litvak, V.D., Colwyn, D.A., Valencia, V.A., Carrasco, M., 2018. The late Oligocene–early Miocene marine transgression of Patagonia, in: The Evolution of the Chilean-Argentinean Andes. Springer, pp. 443–474.

Encinas, A., Folguera, A., Riff, J., Molina, P., Paz, L.F., Litvak, V.D., Colwyn, D.A., Valencia, V.A., Carrasco, M., 2019. Cenozoic basin evolution of the Central Patagonian Andes: Evidence from geochronology, stratigraphy, and geochemistry. *Geoscience Frontiers* 10, 1139–1165.

Escosteguy, L., Dal Molin, C., Franchi, M., Geuna, S., & Lapido, O. (2002). Estratigrafía de la cuenca de los ríos El Zeballos y Jeinemeni, Noroeste de la provincia de Santa Cruz. In Actas del XV Congresso Geológico Argentino. El Calafate.

Escosteguy, L.D., Dal Molin, C.N., Franchi, M., Geuna, S.E., Lapido, O.R., 2003. Hoja Geológica 4772-II Lago Buenos Aires. Servicio Geológico Minero Argentino. Instituto de Geología y Recursos Minerales.

Espinoza, F., Morata Céspedes, D., Polvé, M., Lagabrielle, Y., Maury, R. C., de la Rupelle, A., Guivel, C., Cotten, J., Bellon, H., & Suárez, M. (2010). Middle Miocene calc-alkaline volcanism in Central Patagonia (47° S): Petrogenesis and

implications for slab dynamics Volcanismo calcoalcalino durante el Mioceno Medio en Patagonia Central (47° S): Petrogénesis e implicaciones en la dinámica de placas.

Ethridge, F. G., Wood, L. J., & Schumm, S. A., 1998. Cyclic variables controlling fluvial sequence development: problems and perspectives.

Fernández, M.L., Mazzoli, S., Zattin, M., Savignano, E., Genge, M.C., Tavani, S., Garrone, A., Franchini, M., 2020. Structural controls on Jurassic gold mineralization, and Cretaceous-Tertiary exhumation in the foreland of the southern Patagonian Andes: New constraints from La Paloma area, Deseado Massif, Argentina. *Tectonophysics* 775, 228302.

Fernández Paz, L., Bechis, F., Litvak, V. D., Echaurren, A., Encinas, A., González, J., Lucassen, F., Oliveros, V., Valencia, V. & Folguera, A., 2019. Constraints on trenchward arc migration and backarc magmatism in the North Patagonian Andes in the context of Nazca Plate Rollback. *Tectonics*, 38(11), 3794-3817.

Fernández Paz, L., Iannelli, S.B., Echaurren, A., Ramos, M., Bechis, F., Litvak, V.D., Encinas, A., Kasemann, S., Lucassen, F., Folguera, A., 2020. The late Eocene–early Miocene El Maitén Belt evolution: Magmatic response to the changing subduction zone geodynamics. *Journal of South American Earth Sciences* 102713.

Fernández Paz, L., Litvak, V.D., Echaurren, A., Iannelli, S.B., Encinas, A., Folguera, A., Valencia, V., 2013. Late Eocene volcanism in North Patagonia (42° 30'–43° S): arc resumption after a stage of within-plate magmatism. *Journal of Geodynamics* 113, 13–31.

Feruglio, E., 1949. Descripción geológica de la Patagonia. Casa Editora "Coni".

Figari, C.E., Scasso, R.A., Cúneo, N.R., Escapa, I.H., 2016. Estratigrafía y evolución geológica de la Cuenca de Cañadón Asfalto, Provincia del Chubut, Argentina.

Figari, E., Strelkov, E., Cid de La Paz, M.S., Celaya, J., Laffitte, G., Villar, H., 2002. Cuenca del Golfo San Jorge: Síntesis estructural, estratigráfica y geoquímica, in: *Geología y*

Recursos Naturales de Santa Cruz. Relatorio Del XV Congreso Geológico Argentino.

El Calafate. pp. 571–601.

Figari, E.G., Strelkov, E., Laffitte, G., Cid de La Paz, M.S., Courtade, S.F., Celaya, J., Vottero, A., Lafourcade, P., Martinez, R., Villar, H.J., 1999. Los sistemas petroleros de la Cuenca del Golfo San Jorge: síntesis estructural, estratigráfica y geoquímica, in: 4 Congreso de Exploración y Desarrollo de Hidrocarburos. pp. 197–237.

Fitzgerald, M.G., Mitchum Jr, R.M., Uliana, M.A., Liddle, K.T., 1990. Evolution of the san Jorge basin, Argentina. AAPG bulletin 74, 879–920.

Foix, N., Allard, J.O., Ferreira, M.L., Atencio, M., 2020. Spatio-temporal variations in the Mesozoic sedimentary record, Golfo San Jorge Basin (Patagonia, Argentina): Andean vs. cratonic sources. Journal of South American Earth Sciences 98, 102464.

Foix, N., Paredes, J.M., Giacosa, R.E., 2013. Fluvial architecture variations linked to changes in accommodation space: Río Chico Formation (late Paleocene), Golfo San Jorge basin, Argentina. Sedimentary Geology 294, 342–355.

Foix, N., Paredes, J.M., Giacosa, R.E., 2012. Upper Cretaceous-Paleocene extensional phase in the Golfo San Jorge basin (Argentina): Growth-fault model, paleoseismicity and paleostress analysis. Journal of South American Earth Sciences 33, 110–118.

Folguera, A., Bottesi, G., Duddy, I., Martín-González, F., Orts, D., Sagripanti, L., Vera, E.R., Ramos, V.A., 2015. Exhumation of the Neuquén Basin in the southern Central Andes (Malargüe fold and thrust belt) from field data and low-temperature thermochronology. Journal of South American Earth Sciences 64, 381–398.

Folguera, A., Zárate, M., Tedesco, A., Dávila, F., & Ramos, V. A., 2015. Evolution of the Neogene Andean foreland basins of the Southern Pampas and northern Patagonia (34°–41° S), Argentina. *Journal of South American Earth Sciences*, 64, 452–466.

Folguera, A., Encinas, A., Echaurren, A., Gianni, G., Orts, D., Valencia, V., & Carrasco, G., 2018. Constraints on the Neogene growth of the central Patagonian Andes at the latitude of the Chile triple junction (45–47° S) using U/Pb geochronology in synorogenic strata. *Tectonophysics*, 744, 134–154.

Folguera, A., Paz, L. F., Iannelli, S., Navarrete, C., Echaurren, A., Gianni, G., Butler, K. L., Horton, B. K., Litvak, V., Encinas, A., & Orts, D. (2020). The origin of the San Jorge Gulf Basin in the context of the Mesozoic-Cenozoic evolution of Patagonia. *Journal of South American Earth Sciences*, 97, 102422.

Fosdick, J. C., Grove, M., Graham, S. A., Hourigan, J. K., Lovera, O., & Romans, B. W., 2015. Detrital thermochronologic record of burial heating and sediment recycling in the Magallanes foreland basin, Patagonian Andes. *Basin Research*, 27(4), 546–572.

Fosdick, J. C., Reat, E. J., Carapua, B., Ortiz, G., & Alvarado, P. M. (2017). Retroarc basin reorganization and aridification during Paleogene uplift of the southern central Andes. *Tectonics*, 36(3), 493–514.

Frassinetti, D., Covacevich, V., 1999. Invertebrados fósiles marinos de la Formación Guadal (Oligoceno superior-Mioceno inferior) en Pampa Castillo, región de Aisen, Chile. Servicio Nacional de Geología y Minería.

Garver, J.I., Brandon, M.T., Roden-Tice, M., Kamp, P.J., 1999. Exhumation history of orogenic highlands determined by detrital fission-track thermochronology. Geological Society, London, Special Publications 154, 283–304.

Genge, M., Derycke, A., Gautheron, C., Zattin, M., Witt, C., Mazzoli, S., & Quidelleur, X., 2021a. Tectono-thermal history of the intraplate San Bernardo fold and thrust

belt in central Patagonia inferred by low-temperature thermochronology. *Journal of South American Earth Sciences*, 109, 103333.

Genge, M. C., Zattin, M., Savignano, E., Franchini, M., Gautheron, C., Ramos, V. A., & Mazzoli, S., 2021b. The role of slab geometry in the exhumation of cordilleran-type orogens and their forelands: Insights from northern Patagonia. *Bulletin*, 133(11-12), 2535-2548.

Gehrels, G., 2014. Detrital zircon U–Pb geochronology applied to tectonics. *Annual Review of Earth and Planetary Sciences*, 42, 127-149.

Georgieva, V., Gallagher, K., Sobczyk, A., So'ær, E.R., Schildgen, T.F., Ehlers, T.A., Strecker, M.R., 2019. Effects of slab-window, alkaline volcanism, and glaciation on thermochronometer cooling histories, Patagonian Andes. *Earth and Planetary Science Letters* 511, 164–176.

Georgieva, V., Melnick, D., Schildgen, T.F., Ehlers, T.A., Lagabrielle, Y., Enkelmann, E., Strecker, M.R., 2016. Tectonic control on rock uplift, exhumation, and topography above an oceanic ridge collision: Southern Patagonian Andes (47° S), Chile. *Tectonics* 35, 1317–1341.

Giacosa, R., Zubia, M., Sánchez, M., Allard, J., 2010. Meso-Cenozoic tectonics of the southern Patagonian foreland: Structural evolution and implications for Au–Ag veins in the eastern Deseado Region (Santa Cruz, Argentina). *Journal of South American Earth Sciences* 30, 134–150.

Giacosa, R.E., Franchi, M., Genini, A., Panza, J.L.A., 2001. Hojas Geológicas 4772-III Lago Belgrano y 4772-IV Lago Posadas. Servicio Geológico Minero Argentino. Instituto de Geología y Recursos Minerales.

Giacosa, R.E., Genini, A., 1998. Hoja Geológica 4766-III/IV Puerto Deseado.

Gianni, G.M., Dávila, F.M., Echaurren, A., Fennell, L., Tobal, J., Navarrete, C., Quezada, P., Folguera, A., Giménez, M., 2018. A geodynamic model linking Cretaceous orogeny, arc migration, foreland dynamic subsidence and marine ingressions in southern South America. *Earth-Science Reviews* 185, 437–462.

Gianni, G.M., Echaurren, A., Folguera, A., Likerman, J., Encinas, A., Garcia, H.P.A., Dal Molin, C., Valencia, V.A., 2017. Cenozoic intraplate tectonics in Central Patagonia: Record of main Andean phases in a weak upper plate. *Tectonophysics* 721, 151–166.

Gianni, G.M., Navarrete, C., Orts, D., Tobal, J., Folguera, A., Giménez, M., 2015a. Patagonian broken foreland and related synorogenic rifting: The origin of the Chubut Group Basin. *Tectonophysics* 649, 81–99.

Gianni, G.M., Navarrete, C.G., Folguera, A., 2015b. Synorogenic foreland rifts and transtensional basins: A review of Andean imprints on the evolution of the San Jorge Gulf, Salta Group and Taubaté Basins. *Journal of South American Earth Sciences* 64, 288–306.

Gleadow, A.J.W., 1981. Fission track dating methods: what are the real alternatives? *Nuclear Tracks* 5, 3–14.

Green, P.F., Duddy, I.R., Laslett, G.M., Hegarty, K.A., Gleadow, A.W., Lovering, J.F., 1989. Thermal annealing of fission tracks in apatite 4. Quantitative modelling techniques and extension to geological timescales. *Chemical Geology: Isotope Geoscience Section* 79, 155–182.

Guillaume, B., Gautheron, C., Simon-Labréte, T., Martinod, J., Roddaz, M., Douville, E., 2013. Dynamic topography control on Patagonian relief evolution as inferred from low temperature thermochronology. *Earth and Planetary Science Letters* 364, 157–167.

Guillaume, B., Martinod, J., Husson, L., Roddaz, M., Riquelme, R., 2009. Neogene uplift of central eastern Patagonia: Dynamic response to active spreading ridge subduction? *Tectonics* 28.

Gunther, D. and Heinrich, C.A. (1999). Enhanced sensitivity in LA-ICP-MS using helium-argon mixtures as aerosol carrier. *Journal of Analytical Atomic Spectrometry* 14, 1369–1374

Hamza, V.M., Muñoz, M., 1996. Heat flow map of South America. *Geothermics* 25, 599–646.

Haq, B.U., Hardenbol, J.A.N., Vail, P.R., 1987. Chronology of fluctuating sea levels since the Triassic. *Science* 235, 1156–1167.

Homovc, J.F., Conforto, G.A., Lafourcade, P.A., Chelotti, L.A., 1995. Fold belt in the San Jorge Basin, Argentina: an example of tectonic inversion. Geological Society, London, Special Publications 88, 235–248.

Horton, B.K., 2018. Tectonic regimes of the central and southern Andes: Responses to variations in plate coupling during subduction. *Tectonics* 37, 402–429.

Horton, B.K., Fuentes, F., 2016. Sedimentary record of plate coupling and decoupling during growth of the Andes. *Geology* 44, 647–650.

Horton, B.K., Fuentes, F., Bolívar, A., Starck, D., Ramirez, S.G., Stockli, D.F., 2016. Andean stratigraphic record of the transition from backarc extension to orogenic shortening: A case study from the northern Neuquén Basin, Argentina. *Journal of South American Earth Sciences* 71, 17–40.

Hurford, A.J., 1990. Standardization of fission track dating calibration: Recommendation by the Fission Track Working Group of the IUGS Subcommission on Geochronology. *Chemical Geology: Isotope Geoscience Section* 80, 171–178.

Jackson, S. E., Pearson, N. J., Griffin, W. L., & Belousova, E. A., 2004. The application of laser ablation-inductively coupled plasma-mass spectrometry to in situ U-Pb zircon geochronology. *Chemical geology*, 211(1-2), 47-69.

Jordan, T.E., Isacks, B., Ramos, V.A., Allmendinger, R.W., 1983. Mountain building in the Central Andes. *Episodes* 3, 20–26.

Ketcham, R.A., Carter, A., Donelick, R.A., Barbarand, J., and Hurford, A.J., 2007. Improved modeling of fission-track annealing in apatite: The American Mineralogist , v. 92, p. 799–810, <https://doi.org/10.2138/am.2007.2281>.

Kohn, M. J., Strömberg, C. A., Madden, R. H., Dunn, R. E., Evans, S., Palacios, A., & Carlini, A. A., 2015. Quasi-static Eocene–Oligocene climate in Patagonia promotes slow faunal evolution and mid-Cenozoic global cooling. *Palaeogeography, Palaeoclimatology, Palaeoecology*, 435, 24-37.

Krause, J.M., Bellosi, E.S., 2006. Paleosols from the Koluel Kaire Formation (Lower-Middle Eocene) in the South-central Chubut, Argentina. A preliminary analysis, in: congreso latinoamericano de sedimentología. p. 125.

Legarreta, L., Uliana, M.A., 1994. Asociaciones de fósiles y hiatos en el Supracretácico-Neógeno de Patagonia: una perspectiva estratigráfico-secuencial. *Ameghiniana* 31, 257–281.

Leonard, J.S., Fosdick, J.C., VanderLeest, R.A., 2020. Erosional and Tectonic Evolution of a Retroarc Orogenic Wedge as Revealed by Sedimentary Provenance: Case of the Oligocene–Miocene Patagonian Andes. *Frontiers in Earth Science* 7, 353.

Lesta, P., Ferello, R., 1972. Región extraandina de Chubut y norte de Santa Cruz. *Geología Regional Argentina* 2, 602–687.

Lesta, P., Ferello, R., Chebli, G., 1980. Chubut extraandino, in: Simposio Geología Regional Argentina. Academia Nacional de Ciencias de Córdoba. pp. 1307–1387.

Limarino, C. O., & Giordano, S. R. (2016). Unraveling multiple provenance areas using sandstone petrofacies and geochemistry: An example in the southern flank of the Golfo

San Jorge Basin (Patagonia, Argentina). Journal of South American Earth Sciences, 66, 208–231.

Lizuain, A., Ragona, D., Folguera, A., 1995. Mapa Geológico de la Provincia del Chubut, República Argentina. Secretaría de Minería, Dirección Nacional del Servicio Geológico, Escala 1.

Louterbach, M., Roddaz, M., Antoine, P.-O., Marivaux, L., Adnet, S., Bailleul, J., Dantas, E., Santos, R.V., Chemale Jr, F., Baby, P., 2018. Provenance record of late Maastrichtian–late Palaeocene Andean Mountain building in the Amazonian retroarc foreland basin (Madre de Dios basin, Peru). Terra Nova 30, 17–23.

Maloney, K.T., Clarke, G.L., Klepeis, K.A., Oyarzúedo, L., 2013. The Late Jurassic to present evolution of the Andean margin: Drivers and the geological record. Tectonics 32, 1049–1065.

Malumian, N., Nanez, C., 2011. The Late Cretaceous–Cenozoic transgressions in Patagonia and the Fuegian Andes: foraminifera, palaeoecology, and palaeogeography. Biological Journal of the Linnean Society 103, 269–288.

Malusà, M. G., Anfinsen, O. A., & Stockli, D. F. (2022). (Mis) Identification of magmatic and exhumation ages by detrital zircon UPb and He double dating: A case study from the Bergell-Gonfolite system (European Alps). Chemical Geology, 120970.

Mark, C., Cogné, N., Chew, D., 2016. Tracking exhumation and drainage divide migration of the Western Alps: A test of the apatite U–Pb thermochronometer as a detrital provenance tool. Bulletin 128, 1439–1460.

Marquez, M., & Navarrete, C., 2015. Deformaciones contraccionales previas al Cretácico Superior en la Patagonia Central Argentina. XVI Reunión de Tectónica.

Mpodozis, C., Ramos, V., 1990. The Andes of Chile and Argentina.

Mpodozis, C., Ramos, V.A., 2008. Tectónica jurásica en Argentina y Chile: extensión, subducción oblicua, rifting, deriva y colisiones? Revista de la Asociación geológica Argentina 63, 481–497.

Muñoz, M., 1999. Tectonophysics of the Andes region: relationships with heat flow and the thermal structure, in: International Symposium on Andean Geodynamics. pp. 532–534.

Navarrete, C., Gianni, G., Echaurren, A., Kingler, F.L., Folguera, A., 2016. Episodic Jurassic to lower Cretaceous intraplate compression in Central Patagonia during Gondwana breakup. Journal of Geodynamics 102, 185–201.

Navarrete, C.R., Gianni, G.M., Echaurren, A., Folguera, A., 2018. Lower jurassic to early paleogene intraplate contraction in central Patagonia, in: The Evolution of the Chilean-Argentinean Andes. Springer, pp. 245–271.

Navarrete, C.R., Gianni, G.M., Folguera, A., 2015. Tectonic inversion events in the western San Jorge Gulf Basin from seismic, borehole and field data. Journal of South American Earth Sciences 64, 486–497.

Nie, J., Horton, B.K., Taylor, J.E., Mora, A., Mange, M., Garzione, C.N., Basu, A., Moreno, C.J., Caballero, V., Parra, M., 2012. Integrated provenance analysis of a convergent retroarc foreland system. U–Pb ages, heavy minerals, Nd isotopes, and sandstone compositions of the Middle Magdalena Valley basin, northern Andes, Colombia. Earth-Science Reviews 110, 111–126.

Nullo, F. E., & Combina, A. M., 2002. Sedimentitas terciarias continentales. In Congreso Geológico Argentino (No. 15, pp. 245-258).

Nullo, F., Combina, A., 2011. Patagonian continental deposits (Cretaceous-Tertiary). Biological Journal of the Linnean Society 103, 289–304.

Olazábal, S.X., Tunik, M.A., Paredes, J.M., 2020. Sandstone petrography and provenance of the Chubut Group (Cretaceous) in the Cañadón Matasiete (Golfo San Basin, central Patagonia): Implications for basin evolution and alluvial organization. Journal of South American Earth Sciences 98, 102463.

Orts, D.L., Folguera, A., Encinas, A., Ramos, M., Tobal, J., Ramos, V.A., 2012. Tectonic development of the North Patagonian Andes and their related Miocene foreland basin ($41^{\circ} 30' - 43^{\circ}$ S). Tectonics 31.

Orts, D. L., Folguera, A., Gimenez, M., Ruiz, F., Vera E. A. R., & Klinger, F. L., 2015. Cenozoic building and deformational processes in the North Patagonian Andes. Journal of Geodynamics, 86, 26-41.

Palazzi, L., Barreda, V. D., Cuitiño, J. I., Gurur, M. V., Telleria, M. C., & Ventura Santos, R., 2014. Fossil pollen records indicate that Patagonian desertification was not solely a consequence of Andean uplift. Nature communications, 5(1), 1-8.

Pankhurst, R.J., Weaver, S.D., Hervé, F., Larrondo, P., 1999. Mesozoic-Cenozoic evolution of the North Patagonian batholith in Aysen, southern Chile. Journal of the Geological Society 156, 673–694.

Panza, J.L.A., Cobos, I.C., Zubía, M.A., Franchi, M., 2001a. Hoja Geológica 4769-III Destacamento La María. Servicio Geológico Minero Argentino. Instituto de Geología y Recursos Minerales.

Panza, J.L.A., Genini, A., Franchi, M., 2001b. Hoja Geológica 4769-IV Monumento Natural Bosques Petrificados. Servicio Geológico Minero Argentino. Instituto de Geología y Recursos Minerales.

Panza, J.L.A., Marín, G., Zubía, M.A., 1998. Hoja Geológica 4969-I Gobernador Gregores.

Panza, J.L.A., Márquez, M.J., 1994. Hoja Geológica 4966-I/II Bahía Laura.

Panza, J.L.A., Sacomani, L.E., Cobos, J.C., Asato, C.G., Candaosa, N.G., Chavez, S.B., Gambadé Álvarez, M.L., Olmos, M.I., Tavitian Serrano, A.F., 2003. Mapa geológico de la provincia de Santa Cruz.

Panza, J.L.A., Sacomani, L.E., Giacosa, R.E., Franchi, M., 2018. Hoja Geológica 4972-II Lago Cardiel.

Panza, J.L.A., Zubía, M.A., Godeas, M.C., 1994. Hoja Geológica 4969-II Tres Cerros.

Pardo-Casas, F., Molnar, P., 1987. Relative motion of the Nazca (Farallon) and South American plates since Late Cretaceous time. *Tectonics* 6, 233–248.

Paredes, J.M., Foix, N., Guerstein, G.R., Guler, M.Y., Irigoyen, M., Moscoso, P., Giordano, S., 2015. A late eocene-early Oligocene transgressive event in the Golfo San Jorge basin: Palynological results and stratigraphic implications. *Journal of South American Earth Sciences* 63, 293–309.

Paredes, J.M., Ibañez, L.M., Moyan, M.S., Aceñolaza, G.F., 2009. Sedimentary evolution of the Golfo San Jorge basin, central Patagonia, Argentina, in: Argentinean Fluvial Basins: Ancient and Present Day Examples: Tucumán, Argentina, Excursion Guide Book, 9 International Conference on Fluvial Sedimentology. pp. 187–275.

Parra, M., Mora, A., López, C., Ernesto Rojas, L., Horton, B.K., 2012. Detecting earliest shortening and deformation advance in thrust belt hinterlands: Example from the Colombian Andes. *Geology* 40, 175–178.

Parras, A., Dix, G.R., Griffin, M., 2012. Sr-isotope chronostratigraphy of Paleogene–Neogene marine deposits: Austral Basin, southern Patagonia (Argentina). *Journal of South American Earth Sciences* 37, 122–135.

Parras, A., & Cuitiño, J. I., 2021. Revised chrono and lithostratigraphy for the Oligocene-Miocene Patagoniense marine deposits in Patagonia: Implications for stratigraphic

cycles, paleogeography, and major drivers. *Journal of South American Earth Sciences*, 110, 103327.

Paton, C., Hellstrom, J., Paul, B., Woodhead, J., Hergt, J., 2011. Iolite: Freeware for the visualisation and processing of mass spectrometric data. *Journal of Analytical Atomic Spectrometry* 26, 2508–2518.

Perkins, M. E., Fleagle, J. G., Heizler, M. T., Nash, B., Bown, T. M., Tauber, A. A., & Dozo, M. T. (2012). Tephrochronology of the miocene Santa Cruz and Pinturas formations, Argentina. *Early Miocene Paleobiology in Patagonia: High-Latitude Paleocommunities of the Santa Cruz Formation*. Cambridge University Press, Cambridge, 23-40.

Peroni, G.O., Hegedus, A.G., Cerdan, J., Legarreta, L., Uliana, M.A., Laffitte, G., 1995. Hydrocarbon accumulation in an inner and segment of the Andean Foreland: San Bernardo belt, Central Patagonia.

Petrus, J.A., Kamber, B.S., 2012. VizualAge: A novel approach to laser ablation ICP-MS U-Pb geochronology data reduction. *Geostandards and Geoanalytical Research* 36, 247–270.

Pezzuchi, H.D., 2018. *Boja Geológica 4569-III Sarmiento*.

Raigemborn, M.S., Krause, J.M., Bellosi, E., Matheos, S.D., 2010. Redefinición estratigráfica del grupo Río Chico (Paleógeno Inferior), en el norte de la cuenca del golfo San Jorge, Chubut. *Revista de la Asociación Geológica Argentina* 67, 239–256.

Ramos, V.A., 2014. Evolution of the Golfo San Jorge Basin: structure and tectonic regime. *Revista de la Asociacion Geologica Argentina* 72, 263–282.

Ramos, V.A., 2008. Patagonia: a Paleozoic continent adrift? *Journal of South American Earth Sciences* 26, 235–251.

Ramos, V.A., 2005. Seismic ridge subduction and topography: Foreland deformation in the Patagonian Andes. *Tectonophysics* 399, 73–86.

Ramos, V.A., 1982. Descripción geológica de las Hojas 53 a Monte San Lorenzo y 53 b, Monte Belgrano, Provincia de Santa Cruz. Servicio Geológico Nacional (inéd.), Buenos Aires.

Ramos, V.A., Folguera, A., 2005. Tectonic evolution of the Andes of Neuquén: constraints derived from the magmatic arc and foreland deformation. Geological Society, London, Special Publications 252, 15–35.

Ray, F. M. (1996). Stratigraphical and structural evolution of Tertiary backarc basins in southern Chile (44 deg to 47 deg) (Doctoral dissertation, University of Liverpool).

Ré, G.H., Bellosi, E.S., Heizler, M., Vilas, T.F., Madden, R.H., Carlini, A.A., Kay, R.F., Vucetich, M.G., 2010. A geochronology for the Sarmiento Formation at Gran Barranca. Cambridge University Press Cambridge.

Renda, E.M., Alvarez, D., Prezzi, C., Oriolo, S., Vizán, H., 2019. Inherited basement structures and their influence in foreland evolution: A case study in Central Patagonia, Argentina. *Tectonophysics* 772, 228232.

Roddaz, M., Hermozas, W., Mora, A., Baby, P., Parra, M., Christophoul, F., Brusset, S., Espurt, N., 2010. Cenozoic sedimentary evolution of the Amazonian foreland basin system. *Amazonia, landscape and species evolution: a look into the past*. Blackwell-Wiley, Hoboken 61–88.

Romans, B.W., Fildani, A., Graham, S.A., Hubbard, S.M., Covault, J.A., 2010. Importance of predecessor basin history on sedimentary fill of a retroarc foreland basin: provenance analysis of the Cretaceous Magallanes basin, Chile (50–52 S). *Basin Research* 22, 640–658.

Ruiz, G.M.H., Seward, D., Winkler, W., 2004. Detrital thermochronology—a new perspective on hinterland tectonics, an example from the Andean Amazon Basin, Ecuador. *Basin Research* 16, 413–430.

Savignano, E., Mazzoli, S., Arce, M., Franchini, M., Gautheron, C., Paolini, M., Zattin, M., 2016. (Un) Coupled thrust belt-foreland deformation in the northern Patagonian Andes: New insights from the Esquel-Gastre sector ($41^{\circ} 30'$ – 43° S). *Tectonics* 35, 2636–2656.

Saylor, J. E., Stockli, D. F., Horton, B. K., Nie, J., & Mora, A. (2012). Discriminating rapid exhumation from syndepositional volcanism using detrital zircon double dating: Implications for the tectonic history of the Eastern Cordillera, Colombia. *Bulletin*, 124(5-6), 762-779.

Scalabrino, B., Ritz, J.F., Lagabrielle, Y., 2009. Using glacial morphology to constrain the impact of the Chile active spreading ridge subduction in Central Patagonia, in: EGU General Assembly Conference Abstracts. p. 8518.

Schoene, B., Bowring, S.A., 2005. U-Pb systematics of the McClure Mountain syenite: thermochronological constraints on the age of the 40 Ar/39 Ar standard MMhb. *Contributions to Mineralogy and Petrology* 151, 615.

Sciutto, J.C., Césari, O., Escribano, V., Pezzuchi, H.D., 2000. Hoja Geológica 4566-III Comodoro Rivadavia. Servicio Geológico Minero Argentino. Instituto de Geología y Recursos Minerales.

Sciutto, J.C., Césari, O., Lantanos, N., Ardolino, A.A., 2008. Hoja Geológica 4569-IV Escalante. Servicio Geológico Minero Argentino. Instituto de Geología y Recursos Minerales.

Sharman, G. R., & Malkowski, M. A. (2020). Needles in a haystack: Detrital zircon UPb ages and the maximum depositional age of modern global sediment. *Earth-Science Reviews*, 203, 103109.

Sláma, J., Košler, J., Condon, D. J., Crowley, J. L., Gerdes, A., Hanchar, J. M., Horstwood, M. S.A., Morris, G. A., Nasdala, L., Norberg, N., Schaltegger, U., Schoene, B., Tubrett, M. N. & Whitehouse, M. J. (2008). Plešovice zircon—a new natural reference material for U–Pb and Hf isotopic microanalysis. *Chemical Geology*, 249(1-2), 1-35.

Suárez, M., De La Cruz, R., Etchart, H., Márquez, M.. Fanning, M., 2015. Síntesis de la Cronología Magnética Meso-Cenozoica de Patagonia Central, Aysén, Chile: edades U–Pb SHRIMP, in: XIV Congreso Geológico Chileno, ST-4, pp. 789–792.

Suárez, M., Márquez, M., De La Cruz, R. & Fanning, M. (2009). Aptian-Albian subaerial volcanic rocks in central Patagonia. Divisadero and Chubut Groups. In XII Congreso Geológico Chileno (pp. 1-4). Santiago.

Suárez, D., De La Cruz, S., & Bell, M. (2007). Geología del área Ñireguao-Baño Nuevo, región Aisén del General Carlos Ibáñez del Campo, Escala 1: 100.000.

Suarez, M., Marquez, M., 2007. A Toarcian retro-arc basin of Central Patagonia (Chubut), Argentina: Middle Jurassic closure, arc migration and tectonic setting. *Andean Geology* 34, 63–79.

Sylwan, C.A., 2001. Geology of the Golfo San Jorge Basin, Argentina. *Geología de la Cuenca del Golfo San Jorge, Argentina. Journal of Iberian Geology* 27, 123–158.

Thomson, S.N., 2002. Late Cenozoic geomorphic and tectonic evolution of the Patagonian Andes between latitudes 42 S and 46 S: An appraisal based on fission-track results from the transpressional intra-arc Liquiñe-Ofqui fault zone. *Geological Society of America Bulletin* 114, 1159–1173.

Thomson, S.N., Brandon, M.T., Tomkin, J.H., Reiners, P.W., Vásquez, C., Wilson, N.J., 2010. Glaciation as a destructive and constructive control on mountain building. *Nature* 467, 313.

Thomson, S.N., Gehrels, G.E., Ruiz, J., Buchwaldt, R., 2012. Routine low-damage apatite U–Pb dating using laser ablation–multicollector–ICPMS. *Geochemistry, Geophysics, Geosystems* 13.

Thomson, S.N., Herve, F., Stockhert, B., Brix, M.R., Adriásola, A., 2001. Late cenozoic tectonic and geomorphic evolution of the Patagonian Andes between 42 ° S and 52 ° S, southern Chile assessed using fission-track thermochronology.

Tunik, M.A., Vietto, M.E., Sciutto, J.C., Estrada, E., 2004. Procedencia de areniscas del Grupo Chubut en el área central de la Sierra de San Bernardo. Análisis preliminar. *Revista de la Asociación Geológica Argentina* 59, 601–606.

Umazano, A.M., Bellosi, E.S., Visconti, G., Jalfin, G.A., Melchor, R.N., 2009. Sedimentary record of a Late Cretaceous volcanic arc in central Patagonia: petrography, geochemistry and provenance of fluvial volcaniclastic deposits of the Bajo Barreal Formation, San Jorge Basin, Argentina. *Cretaceous Research* 30, 749–766.

Umazano, A.M., Bellosi, E.S., Visconti, G., Melchor, R.N., 2012. Detecting allocyclic signals in volcaniclastic fluvial successions: Facies, architecture and stacking pattern from the Cretaceous of central Patagonia, Argentina. *Journal of South American Earth Sciences* 40, 94–115.

Vermesch, P., 2018. IsoplotR: A free and open toolbox for geochronology. *Geoscience Frontiers* 9, 1479–1493.

Vermesch, P., 2013. Multi-sample comparison of detrital age distributions. *Chemical Geology* 341, 140–146.

Vermesch, P., Resentini, A., Garzanti, E., 2016. An R package for statistical provenance analysis. *Sedimentary Geology* 336, 14–25.

Wiedenbeck, M. A. P. C., Alle, P., Corfu, F. Y., Griffin, W. L., Meier, M., Oberli, F. V., Von Quadt, A., Roddick, J. C., & Spiegel, W. (1995). Three natural zircon standards for U-Th-Pb, Lu-Hf, trace element and REE analyses. *Geostandards newsletter*, 19(1), 1-23.

Willett, S.D., Brandon, M.T., 2002. On steady states in mountain belts. *Geology* 30, 175–178.

Witt, C., Reynaud, J. Y., Barba, D., Poujol, M., Aizpurua, C., Rivadeneira, M., & Amberg, C. (2019). From accretion to forearc basin initiation: the case of SW Ecuador, Northern Andes. *Sedimentary Geology*, 379, 138-157.

Zattin, M., Andreucci, B., Thomson, S.N., Röhrs, P.W., Talarico, F.M., 2012. New constraints on the provenance of the ANDPIL-AND-2A succession (western Ross Sea, Antarctica) from apatite triple dating. *Geochemistry, Geophysics, Geosystems* 13.

Tables

Table 1. Summary of samples information including location, lithology, formation and stratigraphic ages.

Table 2. Zircon geochronological U–Pb data for grains used to calculated maximum depositional ages indicated in the last column. All data in supplementary material (Table S1).

Table 3. Apatite fission tracks data. Central ages calculated using dosimeter glass CN5 ($\zeta = 346.11 \pm 11.81$) and given with a confidence interval of 1σ . N: number of apatite crystal counted; and ρ : track density (x 105 tracks/cm²); subscripts s, I and d denoted spontaneous, induced and dosimeter respectively; $P(\chi^2)$: probability of obtaining Chi-square value

(probability $> 5\%$ indicates a homogenous population). Samples with a probability $P(\chi^2) < 5\%$ and/or dispersion $> 15\%$ have been analyzed with the binomial peak-fitting method. Cretaceous samples data from Genge et al. (2021b).

Table 4. Apatite isotopic and age data after common Pb-correction with the single-grain AFT cooling age of the corresponding grains. In grey, grains with well constrained Cretaceous ages.

Figures captions

Figure 1. Published apatite ($\text{U}-\text{Th}/\text{He}$ (AHe) and apatite fission-track (AFT) plotted on a simplified topography and tectonic map of the Patagonia ($41 - 50^\circ\text{S}$; Thomson et al., 2001, 2010; Guillaume et al., 2015; Georgieva et al., 2016; Savignano et al., 2016; Fernández et al., 2020; Genge et al., 2021a; Genge et al., 2021b). Areas surrounded by dotted black lines outline the intraplate reliefs belonging to the Patagonian Broken Foreland. White circle indicates the present position of the Chile Triple Junction (Breitsprecher and Thorkelson, 2009).

Figure 2. Geological map of the Central Patagonian Andes. Black squares correspond to main localities. Co: Coyhaique. CR: Comodoro Rivadavia. GG: Gobernador Gregores. PD: Puerto Deseado. PM: Perito Moreno. Sa: Sarmiento. In blue BAGC: Buenos Aires – General Carrera

lake, M: Musters lake, CH: Colhué-Huapi lake. Stars indicate sample location including the four samples from Genge et al. (2021a) in the San Bernardo FTB (MG7, MG9, MG17 and MG20). Yellow and red stars indicating samples used for analysis on apatite: fission tracks only or both fission tracks and U–Pb, respectively; bold contours for samples used for zircon U–Pb analysis. Geological units are described in the legend (Panza and Márquez, 1994; Panza et al., 1994, 1998, 2001a, 2001b, 2003, 2018; Lizuain et al., 1995; Dal Molin, 1998; Giacosa and Genini, 1998; Sciuotto et al., 2000, 2008; Giacosa et al., 2001; Ardolino et al., 2003; Cobos et al., 2003; Escosteguy et al., 2003; Anselmi et al., 2004; Fezzuchi, 2018).

Figure 3. Chronological table for the central Patagonia between 45 and 48°S depicting plate convergence variations (Maloney et al., 2013), slab window events (CTJ for Chile Triple Junction; (Breitsprecher and Thorkelson, 2009; Maloney et al., 2013), stratigraphic log indicating diverse formations found north and south of the San Jorge Gulf Basin (e.g. Gianni et al., 2015a; Aramendía et al., 2019 and references therein), deformation mode along the Andean Cordillera and its foreland (e.g. Horton, 2018b) and volcanic input variations considering formations and distance from the magmatic arc (Foix et al., 2020 and references therein). The central panel is a sketch of the complex tectonic setting in the area during Late Cretaceous (Gianni et al., 2015a); DM: Deseado Massif, RMS: Río Mayo sub-basin, SBFTB: San Bernardo Fold and Thrust Belt, SJGB: San Jorge Gulf Basin. Stars indicate the different Cenozoic formations sampled in this study and Cretaceous formations from Genge et al. (2021a): yellow stars for samples analyzed only with AFT method, red stars for samples analyzed both with AFT and apatite U–Pb dating methods, bold contours for samples analyzed with zircons U–Pb dating method.

Figure 4. Continental upper Eocene – lower Miocene formations. A. Alternating beds of coarsed and thin sandstones of the Sarmiento Formation (MG1). B. San José Formation sandstone sampled in the Cordillera (MG43). C. Thin section photomicrograph of MG1 that evidences deposits enriched in volcanic clasts (V; groundmass +/- phenocrystals) content with few phenocrystals of olivine (Ol) and pyroxene (Px). D to F. Wetherill concordia diagrams showing the youngest dates obtained on zircon crystals of the samples from the Sarmiento (MG1 and MG3) and San José Formations (MG43).

Figure 5. Early Miocene marine formations. A and B. Estuarine cross-bedded sandstones of the Chenque Formation. C. Fossiliferous deposits of the Monte Léon Formation. D. Medium grained sandstones of the Monte Léon Formation. E. Thick deposits of alternating fine to medium grained sandstones of the Chenque Formation. F and G. Thin sections photomicrographs of MG4 and MG6 that evidence a high proportion of volcanic lithic fragments (V; groundmass +/- phenocrystals), with some olivine (Ol) and pyroxene (Px) crystals, and plagioclase (F). Calcitic cement is also evidenced for the sample MG6. H to K. Wetherill concordia diagrams showing the youngest dates obtained on zircon of the samples from the Chenque (MG4 and MG54), Monte León (MG49), and Guadal Formations (MG45).

Figure 6. Early-middle Miocene continental deposits. A. Fluvial cross-bedded deposits of the Santa Cruz Formation. B. Alternance of green and red fluvial beds of the Río Jeinimeni Formation (from the Río Zeballos Group). C. Coarse sandstones intercalated with muddy layers and mud intraclasts of the Pinturas Formation. D and E. Thin section photomicrograph of MG14 and MG16 that illustrates the high volcanic content (V; groundmass +/- phenocrystals) of this formation (mostly altered in MG14) but also some plutonic clasts (G; no groundmass), that are at least partially rounded. Large crystals are mainly feldspars (F) and

quartz (Q). F to H. Wetherill concordia diagrams for zircon grains from the samples MG14, MG16 and MG51. The corresponding ages are similar considering the error margins and yield the youngest ages of 17.5 ± 0.5 Ma

Figure 7. Continental Miocene Río Mayo Formation. A. Alternance of thin and medium grained sandstones. B. Cross-bedded sandstone deposits. C. Thin section photomicrograph of MG11 characterized by various clasts (V and G) and the presence of olivine (Ol), pyroxene (Px), quartz (Q), and feldspars (F) grains is also noticeable. D and E. Wetherill concordia diagrams showing the youngest dates obtained for zircon from the samples MG11 and MG12.

Figure 8. Chubut Group. A and B. Fluvial coarse sandstones with alternating red and green beds from the central (MG20) and the southern (MG7) San Bernardo FTB areas respectively. C and D. Thin sections photomicrograph of MG9 and MG20 show the high volcanic content (V; groundmass +/- phenocrystals) of the Cretaceous formations as well as numerous feldspars (F), quartz (Q) crystals with few plutonic fragments (G; no groundmass), amphibole (A) and micas (M). Most of the volcanic clasts present some alteration. Deformed micas and amphibole have been identified in MG9. E. Wetherill concordia diagram for the sample MG17 showing the youngest date obtained on zircons.

Figure 9. On the left, comparison between Maximum Depositional Ages (MDAs) obtained with zircon U–Pb dating method on different samples with stratigraphic ages from literature (Bridge et al., 2000; De Iuliis et al., 2008; Parras et al., 2012; Dunn et al., 2013; Cuitiño et al., 2015a, 2015b, 2016; Encinas et al., 2019U–Pb). Most samples display MDAs in agreement with the stratigraphic age of the formation except for samples from the Río Mayo and Sarmiento Formations that exhibit older ages. On the right, detrital zircon U–Pb age

distributions that evidence three main volcanism phase during 1) the Miocene, 2) the late Paleogene and 3) the Cretaceous.

Figure 10. Radial plots of single-grain AFT ages arranged according to the different sedimentary formations sampled for this study. Cretaceous samples from the Chubut Group clearly evidence a partial annealing of AFT data (Genge et al., 2021a) while Cenozoic samples show that no significant heating affected those samples. Ages of deposition from Bridge et al., 2000; Blisniuk et al., 2005 ; De Iuliis et al., 2008; Ferras et al., 2012; Dunn et al., 2013; Cuitiño et al., 2015a, 2015b, 2016; Encinas et al., 2019.

Figure 11. A. MDS diagram indicates a clear difference between sediments from all the Miocene formations and the deposits of the San José Formation (beige dashed circle) with the samples from the Sarmiento Formation (brown dashed circle), which appear similar to the Cretaceous samples of the Chubut Group from Genge et al. (2021a) (green dashed circle). The Sicombe-Hazelton distance was used to take in account the analytical uncertainties in the analysis. The axes are corresponding to two dimensional spaces to arrange data. B. Goodness of fit of the MDS plot (Shenard plot).

Figure 12. Apatite U–Pb results. A. All the data together, in red with a robust Cretaceous age, in blue with the more debatable younger population detected. B – F. Populations evidenced for each sample from the Cretaceous Chubut Group (MG20), the early-middle Miocene Chenque Formation (MG4 and MG54), the southern equivalent early Miocene Monte León Formation (MG49) and the Río Mayo Formation (MG12).

Figure 13. A. AFT populations obtained for each sample. B. Sarmiento Formation looks mostly constituted of reworked clasts from the surrounding Cretaceous layers as evidenced by the components P3 and P4, while San José Formation is more composed by volcanic content from the active arc (Fernández Paz et al., 2019). C. Chenque (and equivalents), Santa Cruz and Río Mayo Formations are mostly composed of P1 and P2 peaks representing the ages of the central Patagonian Andes exhumation, coeval with volcanism for the P1 component. P3 peak recorded in one sample may be explained by reworking of surrounding Chubut Group or Sarmiento Formation.

Declaration of interests

The authors declare that they have no known competing financial interests or personal relationships that could have appeared to influence the work reported in this paper.

The authors declare the following financial interests/personal relationships which may be considered as potential competing interests:

Highlights

- Multiproxy provenance study of volcano-sedimentary deposits in San Jorge Basin
- A dominant local source from intraplate belt during late Paleogene
- Cordillera represents the main source for the entire foreland during Miocene times
- Source changes related to a decrease of intraplate reliefs erosion during neutral setting

TABLE 1. SUMMARY OF SAMPLE INFORMATION

Samples	Field			Geology		
	Longitude	Latitude	Elev. (m)	Lithology	Formation	Stratigraphic age
MG1 [#]	-68.8806	-45.7784	395	medium sandstone	Sarmiento	lower Eocene - Oligocene
MG3 [#]	-68.7684	-45.7491	398	sandstone	Sarmiento	lower Eocene - Oligocene
MG4 ^{\$}	-67.8128	-45.8422	367	medium sandstone	upper Chenque	lower-middle Miocene
MG5	-67.9561	-45.8297	610	medium sandstone	Santa Cruz	middle Miocene
MG6	-68.1723	-45.7721	613	medium sandstone	upper Chenque	lower-middle Miocene
MG7*	-69.2818	-45.5345	283	medium sandstone	Bajo Barreal	Cenomanian
MG9*	-69.7016	-45.4590	557	medium sandstone	Castillo	Aptian - Albian
MG11	-70.2658	-45.6747	484	sandstone	Río Mayo	upper Miocene to Pliocene
MG12 ^{\$}	-71.0792	-45.8858	733	sandstone	Río Mayo	upper Miocene to Pliocene
MG13	-71.6418	-46.6084	325	medium sandstone	Río Jemímeni	middle to upper Miocene
MG14 [#]	-71.7229	-46.7390	709	medium sandstone	Cerro Boaleadoras	middle to upper Miocene
MG15	-70.6897	-46.9614	693	medium sandstone	Punturas	middle to upper Miocene
MG16 [#]	-70.8325	-47.1046	700	finesandstone	Punturas	middle to upper Miocene
MG17* [#]	-69.0178	-45.4174	373	fine sandstone	Castillo	Aptian
MG20* [#]	-69.3007	-45.1388	568	medium sandstone	Matasiete	Aptian - Albian
MG43	-72.4984	-46.8012	591	tuffaceous sandstone	San Jose	lower Eocene - Oligocene
MG45 [#]	-72.4951	-46.8204	631	sandstone	Guadal	lower Miocene
MG47	-66.0674	-47.3632	108	fine grained sandstone	Monte León	lower Miocene
MG48	-67.3641	-48.7464	39	sandstone	Monte León	lower Miocene
MG49 ^{\$}	-66.7981	-48.0737	116	sandstone	Monte León	lower Miocene
MG50	-68.7724	-48.5885	189	fine grained sandstone	Chenque	lower Miocene
MG51 [#]	-70.2898	-48.7721	334	sandstone	Santa Cruz	lower Miocene
MG54 ^{\$}	-67.6208	-46.0467	0	sandstone	Chenque	lower-middle Miocene
MG55	-67.4823	-45.7994	36	fine grained sandstone	Sarmiento	lower Eocene - Oligocene

[#]published data (Genge et al., 2021)^{\$}U-Pb analyses on apatite; [#]U-Pb analyses on zircon; ^{\$}U-Pb analyses on both zircon and apatite

TABLE 2. ZIRCON ISOTOPIC AND AGE DATA.

Sample	$^{207}\text{Pb}/$	\pm	^{235}U	\pm	$^{206}\text{Pb}/$	\pm	Rho	Apparent ages (Ma)				MDA (Ma) $\pm (2\sigma)$
	^{206}Pb	(2s)	^{235}U	(2 σ)	^{238}U	(2 σ)		$^{206}\text{Pb}/^{238}\text{U}$	$\pm(2\sigma)$	$^{207}\text{Pb}/^{206}\text{Pb}$	$\pm(2\sigma)$	
MG1_1	0.0463	0.0097	0.0816	0.0166	0.01279	0.00062	0.24	81.9	3.9	11	468	
MG1_2	0.0481	0.0053	0.0847	0.0098	0.01278	0.00040	0.27	81.9	2.5	104	252	82.0 \pm 0.8
MG1_3	0.0466	0.0065	0.0843	0.0114	0.01312	0.00046	0.26	84.0	2.9	27	318	
MG1_11	0.0475	0.0078	0.0815	0.0139	0.01245	0.00052	0.25	79.8	3.3	74	371	
MG3_4	0.0496	0.0076	0.0762	0.0112	0.01113	0.00052	0.32	71.4	3.3	177	341	
MG3_7	0.0492	0.0069	0.0856	0.0116	0.01263	0.00044	0.26	80.9	2.8	157	312	83.4 \pm 0.6
MG3_8	0.0472	0.0082	0.0865	0.0147	0.01328	0.00052	0.23	85.0	3.3	61	391	
MG3_11	0.0481	0.0045	0.0856	0.0077	0.01291	0.00034	0.29	82.7	2.2	104	215	
MG3_12	0.0462	0.0085	0.0818	0.0147	0.01284	0.00052	0.23	82.2	3.3	8	416	
MG4_2	0.0471	0.0121	0.0175	0.0047	0.00269	0.00020	0.28	17.3	1.3	52	563	16.2 \pm 0.6
MG4_3	0.0466	0.0466	0.0143	0.0141	0.00223	0.00040	0.18	14.4	2.6	26	1795	
MG4_4	0.0464	0.0201	0.0143	0.0063	0.00223	0.00022	0.22	14.4	1.4	19	902	

MG4_5	0.0473	0.0321	0.0176	0.0122	0.00270	0.00036	0.19	17.4	2.3	64	1313	
MG4_6	0.0729	0.0293	0.0240	0.0091	0.00238	0.00032	0.35	15.3	2.1	1010	724	
MG4_7	0.0468	0.0187	0.0201	0.0083	0.00311	0.00036	0.28	20.0	2.3	41	837	
MG4_8	0.0471	0.0187	0.0138	0.0053	0.00212	0.00024	0.30	13.7	1.5	56	830	
MG4_10	0.0475	0.0056	0.0177	0.0045	0.00271	0.00060	0.88	17.4	3.9	72	271	
MG4_12	0.0468	0.0196	0.0196	0.0080	0.00304	0.00030	0.24	19.6	1.9	39	875	
MG11_1	0.0459	0.0051	0.0137	0.0018	0.0022	0.0002	0.55	14.0	1.0	-7	250	
MG11_2	0.0503	0.0142	0.0167	0.0048	0.0024	0.0001	0.20	15.5	0.9	208	549	
MG11_3	0.0463	0.0167	0.0163	0.0061	0.0026	0.0002	0.25	16.4	1.5	15	695	16.0 ± 0.4
MG11_4	0.0506	0.0262	0.0174	0.0092	0.0025	0.0002	0.18	16.1	1.5	221	893	
MG11_5	0.0509	0.0072	0.0199	0.0030	0.0028	0.0002	0.37	18.2	1.0	235	298	
MG11_6	0.0475	0.0254	0.0175	0.0095	0.0027	0.0002	0.16	17.2	1.5	77	937	
MG12_1	0.0468	0.0447	0.0161	0.0151	0.00249	0.00040	0.17	16.1	2.6	39	1729	
MG12_3	0.1441	0.0314	0.0478	0.0089	0.00241	0.00028	0.62	15.5	1.8	2277	353	
MG12_5	0.0480	0.0306	0.0142	0.0094	0.00214	0.00042	0.29	15.5	2.7	99	1237	
MG12_7	0.0473	0.0408	0.0156	0.0140	0.00239	0.00060	0.28	14.4	3.9	65	1589	
MG12_8	0.0464	0.0154	0.0140	0.0045	0.00219	0.00020	0.29	14.1	1.3	21	712	
MG12_13	0.0455	0.0157	0.0139	0.0046	0.00221	0.00018	0.24	14.2	1.2	-30	746	14.8 ± 0.2
MG12_18	0.0507	0.0062	0.0167	0.0022	0.00239	0.00012	0.38	15.4	0.8	226	273	
MG12_19	0.0476	0.0088	0.0170	0.0033	0.00259	0.00066	0.32	16.7	1.0	81	412	
MG12_20	0.0474	0.0292	0.0142	0.0085	0.00218	0.00050	0.23	14.0	1.9	70	1209	
MG12_21	0.0466	0.0176	0.0163	0.0064	0.00254	0.00028	0.28	16.4	1.8	31	798	
MG12_22	0.0470	0.0039	0.0151	0.0012	0.00231	0.00006	0.34	15.0	0.4	48	191	
MG12_23	0.0465	0.0041	0.0138	0.0011	0.00215	0.00006	0.34	13.8	0.4	22	204	
MG14_1	0.0423	0.0226	0.0152	0.0080	0.00261	0.00026	0.19	16.8	1.7	-210	1127	
MG14_2	0.0463	0.0063	0.0173	0.0022	0.00271	0.00010	0.29	17.4	0.6	15	311	
MG14_4	0.0488	0.0157	0.0210	0.0064	0.00312	0.00030	0.32	20.1	1.9	140	677	17.8 ± 0.4
MG14_5	0.0470	0.0120	0.0177	0.0044	0.00273	0.00018	0.27	17.6	1.2	48	560	
MG14_6	0.0473	0.0069	0.0178	0.0026	0.00288	0.00014	0.35	18.5	0.9	62	331	
MG14_11	0.0481	0.0156	0.0178	0.0054	0.00262	0.00024	0.29	16.9	1.5	103	690	
MG16_1	0.0479	0.0459	0.0100	0.0184	0.00295	0.00052	0.19	19.0	3.3	96	1717	
MG16_2	0.0470	0.0134	0.0173	0.0048	0.00266	0.00018	0.25	17.1	1.2	51	618	
MG16_3	0.0481	0.0102	0.0231	0.0047	0.00348	0.00022	0.31	22.4	1.4	106	465	
MG16_4	0.0465	0.0122	0.0172	0.0044	0.00268	0.00016	0.23	17.3	1.0	25	575	
MG16_5	0.0472	0.0210	0.0153	0.0066	0.00235	0.00028	0.28	15.1	1.8	59	918	
MG16_8	0.0477	0.0239	0.0176	0.0086	0.00268	0.00028	0.21	17.3	1.8	84	1012	
MG16_9	0.0490	0.0219	0.0200	0.0087	0.00296	0.00034	0.27	19.1	2.2	149	907	17.8 ± 0.4
MG16_10	0.0468	0.0196	0.0176	0.0071	0.00273	0.00028	0.25	17.6	1.8	37	874	
MG16_13	0.0479	0.0190	0.0206	0.0079	0.00312	0.00028	0.23	20.1	1.8	92	826	
MG16_14	0.0464	0.0246	0.0198	0.0102	0.00309	0.00040	0.25	19.9	2.6	16	1077	
MG16_15	0.0486	0.0140	0.0184	0.0051	0.00275	0.00022	0.29	17.7	1.4	130	615	
MG16_18	0.0481	0.0176	0.0201	0.0072	0.00303	0.00026	0.24	19.5	1.7	105	768	
MG16_19	0.0475	0.0249	0.0199	0.0108	0.00304	0.00042	0.25	19.6	2.7	75	1056	
MG16_25	0.0464	0.0133	0.0174	0.0048	0.00273	0.00022	0.29	17.6	1.4	17	626	
MG16_28	0.0475	0.0203	0.0172	0.0076	0.00263	0.00028	0.24	16.9	1.8	75	885	

MG16_31	0.0456	0.0161	0.01504	0.0052	0.00239	0.00018	0.22		15.4	1.2	-23	760	
MG17_3	0.0478	0.0022	0.1049	0.0046	0.01592	0.00026	0.37		101.8	1.6	90	109	
MG17_7	0.0481	0.0025	0.1069	0.0054	0.01612	0.00028	0.35		103.1	1.8	105	122	103.1 ± 0.5
MG17_8	0.0503	0.0051	0.1119	0.0109	0.01614	0.00048	0.31		103.2	3.0	208	227	
MG17_10	0.0492	0.0031	0.1115	0.0067	0.01644	0.00034	0.34		105.1	2.2	158	145	
MG43_1	0.0503	0.0077	0.0442	0.0070	0.0064	0.0002	0.24		40.9	1.5	208	321	
MG43_2	0.0461	0.0017	0.0448	0.0018	0.0071	0.0001	0.43		45.3	0.8	2	85	
MG43_3	0.0527	0.0304	0.0400	0.0231	0.0055	0.0002	0.05		35.4	1.1	314	955	
MG43_4	0.0494	0.0142	0.0336	0.0099	0.0049	0.0003	0.22		31.7	2.1	166	561	
MG43_5	0.0472	0.0096	0.0402	0.0084	0.0062	0.0003	0.23		39.7	1.9	59	425	
MG43_6	0.0560	0.0110	0.0372	0.0077	0.0048	0.0003	0.33		31.0	2.1	454	385	40.4 ± 0.4
MG43_7	0.0445	0.0073	0.0341	0.0057	0.0056	0.0002	0.22		35.7	1.3	-85	360	
MG43_8	0.0469	0.0096	0.0349	0.0073	0.0054	0.0003	0.22		34.7	1.6	46	428	
MG43_9	0.0487	0.0052	0.0439	0.0054	0.0066	0.0004	0.50		42.1	2.6	132	232	
MG43_10	0.0502	0.0033	0.0418	0.0034	0.0061	0.0003	0.56		38.7	1.7	202	148	
MG43_11	0.0469	0.0082	0.0499	0.0089	0.0077	0.0003	0.24		40.5	2.1	44	371	
MG43_12	0.0518	0.0038	0.0505	0.0042	0.0071	0.0003	0.49		45.4	1.8	276	158	
MG43_13	0.0507	0.0047	0.0362	0.0036	0.0052	0.0002	0.35		33.3	1.1	229	201	
MG45_1	0.0482	0.0128	0.0199	0.0051	0.00299	0.00022	0.25		19.2	1.4	111	573	
MG45_2	0.0464	0.0436	0.0202	0.0186	0.00316	0.0000	0.21		20.3	3.9	16	1715	
MG45_5	0.0475	0.0529	0.0165	0.0189	0.00252	0.00000	0.23		16.2	4.2	76	1929	
MG45_6	0.0496	0.0229	0.0202	0.0091	0.00295	0.00032	0.24		19.0	2.1	178	929	
MG45_8	0.0495	0.0121	0.0216	0.0056	0.0031	0.00024	0.29		20.4	1.5	172	527	19.8 ± 0.6
MG45_11	0.0479	0.0455	0.0208	0.0203	0.00315	0.00068	0.22		20.3	4.4	94	1706	
MG45_16	0.0474	0.0266	0.0211	0.0114	0.00323	0.00048	0.27		20.8	3.1	68	1120	
MG45_19	0.0471	0.0137	0.0199	0.0051	0.00306	0.00030	0.32		19.7	1.9	52	631	
MG45_20	0.0470	0.0163	0.0212	0.0076	0.00327	0.00030	0.26		21.0	1.9	48	740	
MG45_22	0.0467	0.0214	0.0194	0.0086	0.00301	0.00032	0.24		19.4	2.1	33	946	
MG45_28	0.0466	0.0129	0.0121	0.0052	0.00305	0.00024	0.30		19.6	1.5	28	605	
MG49_3	0.0467	0.0186	0.0201	0.0077	0.00318	0.00038	0.32		20.5	2.4	34	835	
MG49_4	0.0477	0.0102	0.0210	0.0050	0.00334	0.00024	0.32		21.5	1.5	82	473	20.8 ± 0.9
MG49_8	0.0477	0.0130	0.0205	0.0058	0.00311	0.00024	0.27		20.0	1.5	85	590	
MG49_10	0.0469	0.0252	0.0215	0.0120	0.00333	0.00048	0.26		21.4	3.1	46	1080	
MG51_1	0.0452	0.0096	0.0164	0.0034	0.00264	0.00016	0.30		17.0	1.0	-48	480	
MG51_3	0.0465	0.0279	0.0169	0.0103	0.00264	0.00026	0.16		17.0	1.7	25	1193	
MG51_4	0.0439	0.0296	0.0161	0.0110	0.00266	0.00026	0.14		17.1	1.7	-115	1343	17.5 ± 0.5
MG51_9	0.0497	0.0206	0.0182	0.0078	0.00266	0.00026	0.23		17.1	1.7	181	844	
MG51_10	0.0478	0.0124	0.0180	0.0045	0.00273	0.00016	0.23		17.6	1.0	88	562	
MG51_13	0.0471	0.0123	0.0185	0.0050	0.00285	0.00016	0.21		18.3	1.0	54	571	
MG51_14	0.0454	0.0160	0.0174	0.0063	0.00279	0.00022	0.22		18.0	1.4	-36	763	
MG54_1	0.0500	0.0155	0.0162	0.0048	0.00235	0.00022	0.32		15.1	1.4	196	649	
MG54_3	0.0463	0.0105	0.0175	0.0038	0.00275	0.00020	0.34		17.7	1.3	12	504	18.0 ± 0.4
MG54_5	0.0467	0.0093	0.0175	0.0033	0.00271	0.00016	0.31		17.4	1.0	34	445	
MG54_11	0.0495	0.0236	0.0188	0.0094	0.00276	0.00042	0.30		17.8	2.7	173	954	
MG54_13	0.0473	0.0152	0.0177	0.0055	0.00271	0.00024	0.29		17.4	1.5	63	686	

MG54_14	0.0455	0.0130	0.0168	0.0046	0.00267	0.00020	0.27		17.2	1.3	-27	629	
MG54_17	0.0485	0.0336	0.0179	0.0128	0.00267	0.00048	0.25		17.2	3.1	126	1320	
MG54_18	0.0466	0.0179	0.0186	0.0069	0.00289	0.00028	0.26		18.6	1.8	31	809	
MG54_20	0.0521	0.0119	0.0234	0.0051	0.00326	0.00022	0.31		21.0	1.4	291	483	
MG54_21	0.0475	0.0110	0.0182	0.0044	0.00278	0.00020	0.30		17.9	1.3	75	507	
MG54_22	0.0472	0.0286	0.0181	0.0106	0.00277	0.00040	0.25		17.8	2.6	57	1195	
MG54_24	0.0465	0.0239	0.01978	0.0100	0.00309	0.00032	0.21		19.9	2.1	22	1048	
MG54_27	0.0473	0.0097	0.01803	0.0035	0.00277	0.00016	0.29		17.8	1.0	62	455	
MG54_28	0.0474	0.0289	0.01596	0.0095	0.00244	0.00030	0.21		15.7	1.9	71	1197	
MG54_30	0.0471	0.0155	0.01864	0.0059	0.00287	0.00024	0.26		18.5	1.5	52	703	
MG54_31	0.0491	0.0072	0.0199	0.0031	0.00294	0.00014	0.31		18.9	0.9	151	328	

*: stands for grains excluded from the age calculation (igneous samples) or from the probability density plots (sedimentary samples). In the latter case, rejection was based on a 10% discordance threshold calculated from the distance to concordia.

TABLE 3. SUMMARY OF APATITE FISSION TRACKS DATA

Samples [†]	Fission tracks data								< 40 Ma			40 - 65 Ma			65 - 150 Ma			> 150 Ma						
	n	C. age	σ	N s	p s	Ni	p i	Nd	p D	Dis p. (%)	P(x ²)	P 1	σ	%	P 2	σ	%	P 3	σ	%	P4	σ	%	
MG1	4 9	72. 5	5. 8	# #	2	## ##	5	## ##	# #	28	21							# #	# #	9 4	## ##	# #	6 6	
MG3	4 8	74. 4	7. 3	# #	3	## ##	5	## ##	# #	43	0.0							# #	# #	8 4	## ##	# #	1 6	
MG4	4 8	32. 0	2. 3	# #	1	## ##	6	## ##	# #	0	##	# #	# #	# #	# #	# #	# #	# #	# #	# #	# #	# #		
MG5	1 8	33. 9	4. 1	5 5	1	31 6	5	## ##	# #	1	86. 7	# #	# #	# #	# #	# #	# #	# #	# #	# #	# #	# #		
MG6	1 7	51. 7	7. 5	6 2	1	27 5		## ##	# #	0	##						# #	7. 0	# #					
MG7	2 0	88. 5	# #	9 7	1	20 q	3	## ##	# #	0	##													
MG9	1 0	92. 6	# #	8 8		17 8	5	## ##	# #	0	##													
MG11	1 6	44. 4	4. 3	# #	2	72 8	7	## ##	# #	8	92. 0						# #	4. 0	# #					
MG12	5 7	32. 6	3. 2	# #	1	## ##	9	## ##	# #	44	0.0	# #	# #	# #	# #	# #	# #	8. 7	# #	3 8				
MG13	3 4	31. 4	3. 6	# #	1	85 1	0	## ##	# #	0	##	# #	# #	# #	# #	# #	# #	# #	# #	# #	# #	# #		
MG14	2 5	31. 7	3. 2	# #	1	79 0	6	## ##	# #	7	78. 0	# #	# #	# #	# #	# #	# #	# #	# #	# #	# #	# #		
MG15	5 3	38. 9	3. 5	# #	1	97 0	5	## ##	# #	2	91. 6	# #	# #	# #	# #	# #	# #	# #	# #	# #	# #	# #		
MG16	4 1	34. 4	3. 0	# #	1	91 6	5	## ##	# #	9.	97. 0	# #	# #	# #	# #	# #	# #	# #	# #	# #	# #	# #		
MG17*	1 1	96. 7	# #	8 3	1	14 3	2	## ##	9. 7	0	##													

MG2 0*	5 3	### ##	8. 7	# #	3 #	84 7	5 ##	# #	0 ##					
MG4 3	5 9	35. 9	3. 8	# #	1 #	61 8	2 ##	# #	0 ##	# #	# #	# #	# #	
MG4 5	5 4	26. 5	2. 2	# #	1 ##	## 8	## #	9. 9	10 0	97. 0	# #	# #	# #	
MG4 7	5 4	55. 4	3. 9	# #	2 ##	## 5	## #	# #	0 ##		# #	3. 4	# #	
MG4 8	6 3	31. 4	2. 7	# #	1 #	63 5	7 ##	# #	57 #	5.0 #	# #	9 4	# #	
MG4 9	6 7	43. 5	3. 2	# #	3 ##	## #	## #	# #	25 #	26. 3	# #	5 0	# #	
MG5 0	3 9	39. 8	3. 6	# #	2 ##	## #	## #	# #	0 ##		# #			
MG5 1	# #	23. 5	1. 6	# #	1 ##	## 5	## #	# #	13 #	59. 8	# #	# #	# #	
MG5 4	5 2	43. 4	3. 7	# #	2 ##	## #	## #	# #	40 #	0.0 #	# #	2 #	# #	
MG5 5	2 2	91. 5	7. 3	# #	5 2	59 9	## ##	# #	0 #	10 0				

† Zeta= 346 ± 12 using dosimeter glass CNS

N: number of apatite crystal counted; and p: track density ($\times 10^5$ tracks/ cm^{-2}), subscripts s, l and d denote spontaneous, induced and dosimeter, respectively; P(χ^2): probability of obtaining a Chi-square value for n degrees of freedom, samples with a probability $P(\chi^2) < 5\%$ and/or dispersion > 15% have been analysed with the binomial peak-fitting method.

*published data (Genge et al., 2021)

TABLE 4. SINGLE GRAIN APATITES U-PB AND AFT DATA

Sam- ples	^{207}P b / ^{235}U	\pm 2σ	^{206}P b / ^{238}U	\pm 2σ	^{238}U / ^{206}P	^{207}P b / ^{206}P	\pm 2σ	U b	(pp m)	Th (pp m)	Pb (pp m)	U/T h	^{207}Pb corr. age	\pm 2σ	S&K val- ue (5th it.)	AFT age (Ma)	2σ
McClur e_1	3.27 0	### #	0.1 06	## #	9. #	### #	0.2 20	## #	### ##	32.6 4	3.02 0	0.44 2	531 44				
McClur e_2	2.71 0	### #	0.1 01	## #	9.88 1	### #	0.1 90	## #	### ##	91.8 0	7.13 0	0.32 6	526 41				
McClur e_3	3.91 0	### #	0.1 10	## #	9.13 2	### #	0.2 52	## #	### ##	57.8 0	4.43 0	0.29 7	518 40				
McClur e_4	4.89 0	### #	0.1 24	## #	8.08 4	### #	0.3 05	## #	### ##	20.5 0	2.49 0	0.56 7	535 57				
McClur e_5	2.19 0	### #	0.0 97	## #	### #	## #	0.1 62	## #	### ##	40.5 0	3.11 0	0.50 6	522 46				
MG54_ 1	1.69 0	### #	0.0 33	## #	### #	## #	0.3 89	## #	### ##	16.5 1	3.35 0	3.51 0	118.6 9.2	0.84	31. 33	27. 07	18
MG54_ 2	### ##	### #	0.0 90	## #	### #	## #	0.8 80	## #	### ##	1.48 #	4.56 #	0.52 9	-34.4 #	0.83	55. 34	71. 57	86
MG54_ 3	### ##	### #	0.1 71	## #	5.84 8	## #	0.8 03	## #	### ##	2.44 #	8.18 #	1.69 9	49.7 #	0.83	37. 88	56. 1	74
MG54_ 4	0.58 7	### #	0.0 21	## #	## #	## #	0.2 07	## #	## ##	2.48 #	2.48 4	0.72 6	105.2 5.5	0.84	22. 24	13. 86	96
MG54_ 5	2.19 0	### #	0.0 36	## #	## #	## #	0.4 16	## #	## ##	9.60 #	2.99 #	4.15 6	122.9 7	0.84	92. 36	42. 07	7
MG54_ 6	2.80 0	### #	0.0 30	## #	## #	## #	0.7 01	## #	## ##	6.54 #	25.9 4	0.26 6	33.6 2	0.83	37. 78	26. 1	86
MG54_ 7	7.39 0	### #	0.0 77	## #	## #	## #	0.7 04	## #	## ##	9.29 0	27.1 0	0.36 4	84.6 5	0.84	30. 11	16. 37	86

MG54_8	9.33	###	0.0	###	###	###	0.9	###	3.89	13.7	1.44	0.29	-51.4	45.	0.83	21.	17.	
MG54_9	3.61	###	0.0	###	###	###	0.5	###	###	27.0	2.85	0.73	116.0	14.	0.84	26.	21.	
MG54_10	5.99	###	0.0	###	###	###	0.6	###	###	26.3	2.93	0.53	98.8	22.	0.84	52.	52.	
MG54_11	7.10	###	0.0	###	###	###	0.6	###	###	34.4	3.11	0.30	112.5	20.	0.84	52.	52.	
MG54_12	9.30	###	0.0	###	###	###	0.8	###	5.03	17.0	1.88	0.30	0.4	43.	0.83	23.	28.	
	0	#	84	#	#	#	35	#	7	7	4		8	56	05	02		
MG4_1	6.88	###	0.0	###	###	###	0.8	###	4.82	10.8	1.13	0.39	9.7	36.	0.83	22.	12.	
MG4_2	0	#	59	#	#	#	16	#	7	3			7	62	12	2		
MG4_3	###	###	0.2	###	3.63	###	0.8	###	1.41	4.54	1.47	0.26	-69.7	###	0.83	28.	35.	
MG4_4	##	#	75	#	6	#	62	#					#	12	63	64		
MG4_5	###	###	0.1	###	5.06	###	0.8	###	4.13	6.72	3.08	0.51	-13.3	77.	0.83	38.	14.	
MG4_6	##	#	98	#	3	#	43	#					2	48	14	26		
MG4_7	##	#	97	#	#	#	65	#	8.37	12.2	3.15	0.56	58.6	32.	0.83	47.	43.	
MG4_8	##	#	97	#	#	#	65	#					3	94	23	44		
MG4_9	##	#	33	#	8	#	20	#	6.08	9.21	3.08	0.53	18.2	46.	0.83	47.	43.	
MG4_10	##	#	0.1	###	6.74	###	0.7	###	3.53	10.3	1.93	0.26	49.0	82.	0.83	29.	28.	
MG4_11	##	#	48	#	3	#	98	#					2	88	24	26		
MG4_12	##	#	0.1	###	5.46	###	0.8	###	3.06	9.84	1.11	0.34	-37.1	80.	0.83	41.	37.	
MG4_13	##	#	83	#	4	#	58	#					9	33	8	98		
MG4_14	##	#	0.1	###	5.98	###	0.8	###	2.76	5.78	1.10	0.34	-32.1	88.	0.83	36.	32.	
MG4_15	##	#	67	#	1	#	57	#					5	36	24	52		
MG4_16	##	#	0.1	###	5.58	###	0.8	###	2.88	10.03	2.03	0.34	-0.6	71.	0.83	27.	16.	
MG4_17	##	#	79	#	7	#	36	#					3	56	09	24		
MG4_18	##	#	0.1	###	6.25	###	0.8	###	3.17	6.64	1.91	0.33	-0.5	67.	0.83	27.	16.	
MG4_19	##	#	60	#	4	#	36	#					5	56	09	24		
MG4_20	##	#	50	#	0	#	66	#					7	61	19	12		
MG4_21	5.39	###	0.0	###	###	###	0.6	###	###	98.3	4.82	0.16	90.0	15.	0.84	33.	15.	
MG4_22	0	#	60	#	#	#	54	#					2	14	72	2		
MG12_13	###	###	0.2	###	3.84	###	0.8	###	2.14	3.91	2.10	0.37	-0.9	###	0.83	22.	14.	
MG12_14	1.42	###	0.0	###	###	###	0.3	###	###	37.5	1.75	0.55	103.5	9.0	0.84	11.	10.	
MG12_15	0	#	27	#	#	#	7	#	##	0	1.75	8	51	23	51	58		
MG12_16	###	###	0.1	###	7.53	###	0.9	###	7.22	14.3	3.65	0.34	-21.5	45.	0.83	24.	23.	
MG12_17	##	#	33	#	6	#	54	#					6	43	74	38		
MG12_18	###	###	0.2	###	4.82	###	0.8	###	7.00	18.6	5.62	0.25	-85.2	54.	0.83	23.	14.	
MG12_19	##	#	07	#	2	#	30	#					2	03	55	38		
MG12_20	###	###	0.6	###	1.62	###	0.8	###	1.94	5.55	4.64	0.24	-90.0	###	0.83	45.	70.	
MG12_21	##	#	16	#	3	#	48	#					7	03	45	5		
MG12_22	###	###	0.1	###	6.68	###	0.8	###	3.57	10.8	2.02	0.23	-9.8	63.	0.83	16.	33.	
MG12_23	##	#	50	#	1	#	43	#					3	50	27	7		
MG12_24	###	###	0.2	###	7.96	###	0.8	###	3.65	12.5	3.50	0.21	-63.0	###	0.83	47.	42.	
MG12_25	##	#	52	#	1	#	62	#					8	17	01	32		
MG12_26	###	###	0.1	###	0.07	###	0.9	###	2.85	8.33	1.55	0.26	-83.6	79.	0.83	32.	26.	
MG12_27	##	#	41	#	7	#	02	#					6	03	5	38		
MG12_28	###	###	0.0	###	###	###	0.8	###	2.81	7.60	0.98	0.29	-32.2	76.	0.83	49.	48.	
MG12_29	##	#	85	#	#	#	80	#					7	36	39	88		
MG12_30	###	###	0.0	###	###	###	0.8	###	5.86	21.2	2.24	0.23	-13.9	35.	0.83	19.	20.	
MG12_31	##	#	98	#	#	#	52	#					4	47	38	24		
MG12_32	###	###	0.1	###	8.51	###	0.8	###	7.62	13.6	3.28	0.49	-17.8	44.	0.83	53.	59.	
MG12_33	##	#	18	#	1	#	53	#					1	45	44	52		
MG49_29	###	###	0.1	###	7.49	###	0.8	###	2.73	9.46	1.50	0.69	34.5	73.	0.83	27.	21.	
MG49_30	7.86	###	0.0	###	###	###	0.8	###	5.41	20.9	1.43	0.65	22.4	52.	0.83	37.	41.	
MG49_31	6.51	###	0.0	###	###	###	0.7	###	3.36	9.83	0.80	0.89	60.5	53.	0.83	36.	30.	
MG49_32	8.61	###	0.0	###	###	###	0.8	###	11.1	12.4	4.44	0.89	-8.1	17.	0.83	25.	18.	
MG49_33	3.98	###	0.0	###	###	###	0.8	###	50.1	1.61	0	0.61	-1.0	16.	0.83	30.	33.	
MG49_34	5.95	###	0.0	###	###	###	0.8	###	30.5	2.21	0	0.99	-16.5	26.	0.83	31.	24.	
MG49_35	7.66	###	0.0	###	###	###	0.7	###	4.24	13.0	1.27	0.82	44.9	38.	0.83	44.	99.	
MG49_36	0	#	77	#	#	#	67	#					2	85	41	36		
MG49_37	2.40	###	0.0	###	###	###	0.4	###	###	78.1	3.92	1.29		115.8	10.	0.84	29.	20.

36	0	#	38	#	##	#	62	#	##	0		1		4	31	64	36	
MG49_	9.49	###	0.1	###	###	###	0.6	###	###	49.3	4.12	0.51		116.2	28.	0.84	33.	37.
37	0	#	00	#	#	#	98	#	#	0		4		8	31	86	04	
MG49_	9.60	###	0.0	###	###	###	0.8	###	3.87	13.3	1.40	0.61		8.4	69.	0.83	16.	33.
38	0	#	92	#	#	#	25	#		2		3		3	62	18	82	
MG49_	6.66	###	0.0	###	###	###	0.6	###	###	36.6	3.62	0.73		116.1	26.	0.84	30.	24.
39	0	#	77	#	#	#	55	#	#	0		8		7	31	36	94	
MG49_	4.92	###	0.0	###	###	###	0.6	###	###	32.4	5.67	1.82		106.4	16.	0.84	37.	41.
40	0	#	59	#	#	#	20	#	#	0		4		1	25	42	26	
MG49_	2.72	###	0.0	###	###	###	0.7	###	###	42.3	2.48	1.01		25.7	13.	0.83	20.	12.
41	0	#	28	#	#	#	23	#	#	0		5		7	73	18	92	
MG49_	###	###	0.1	###	9.14	###	0.8	###	4.21	12.5	1.86	0.52		7.2	50.	0.83	31.	24.
42	##	#	09	#	1	#	28	#		5		1		5	61	61	36	
MG49_	###	###	0.1	###	9.42	###	0.8	###	4.43	13.6	1.84	0.47		-28.0	77.	0.83	22.	14.
43	##	#	06	#	5	#	66	#		3		4		0	38	76	68	
MG20_	###	###	0.2	###	4.93	###	0.7	###	###	2.39	0.46			140.8	72.	0.84	136	125
24	##	#	03	#	6	#	58	#	#	2		7		45	7	48	.2	.9
MG20_	###	###	0.1	###	5.78	###	0.7	###	###	2.27	0.45			123.0	81.	0.84	75.	122
25	##	#	73	#	0	#	55	#	#	0		2		92	6	36	13	.8
MG20_	###	###	0.1	###	6.86	###	0.7	###	###	4.95	0.47			121.0	39.	0.84	112	112
27	##	#	46	#	8	#	40	#	#	0				08	2	35	.4	.7

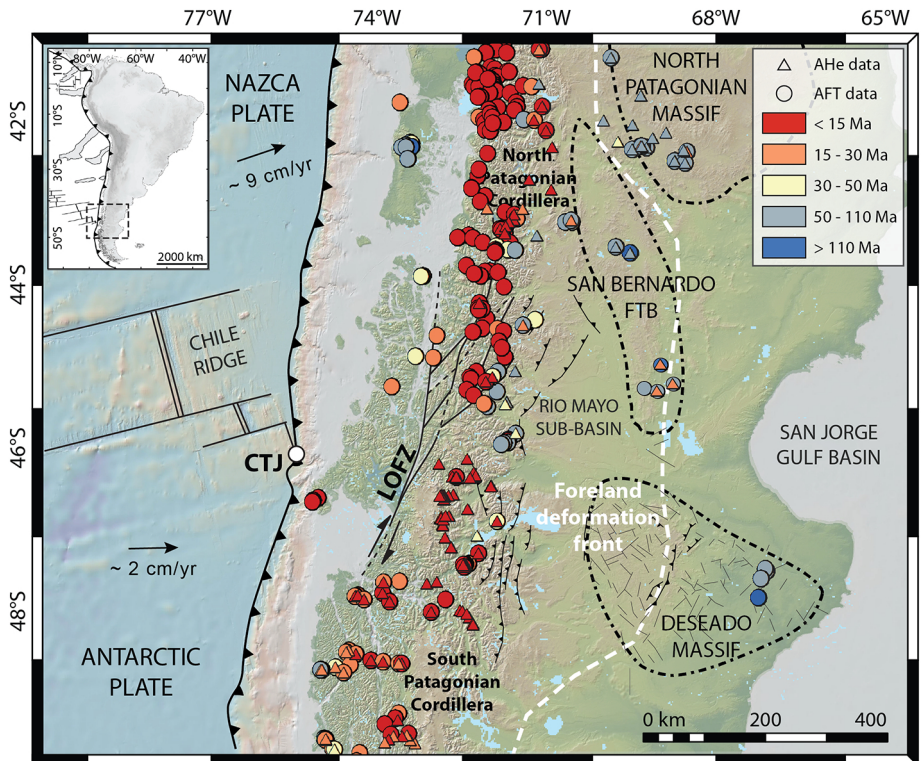


Figure 1

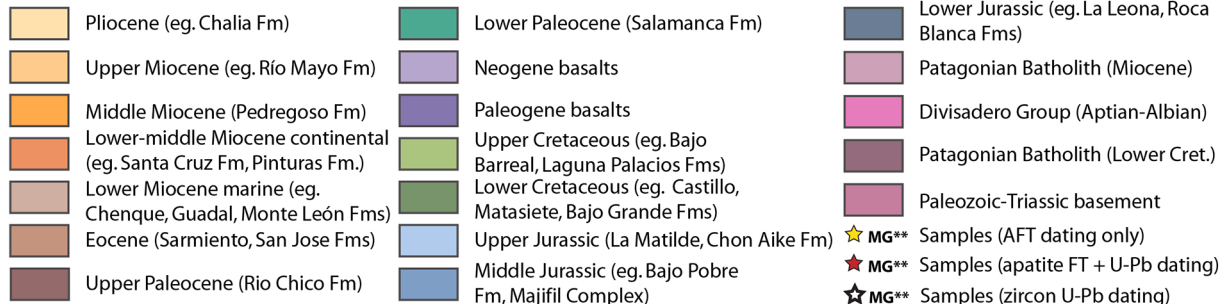
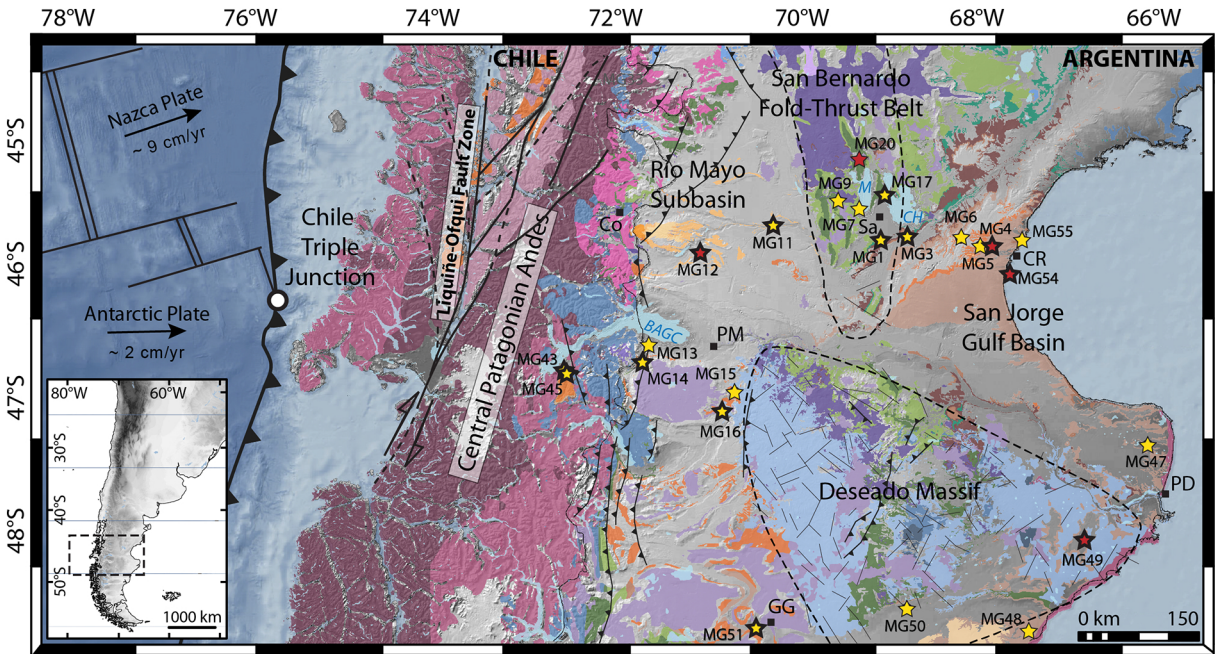


Figure 2

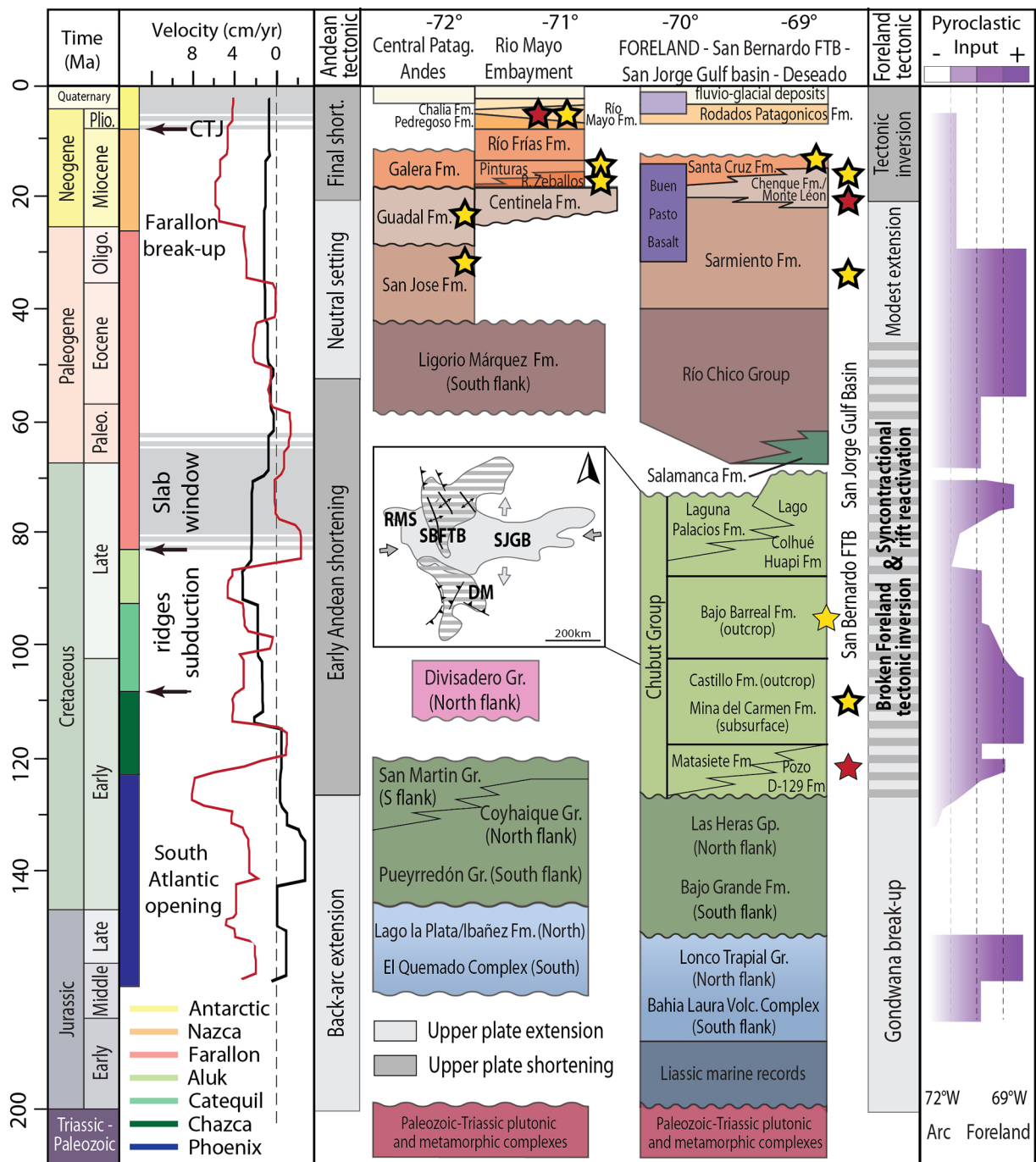


Figure 3

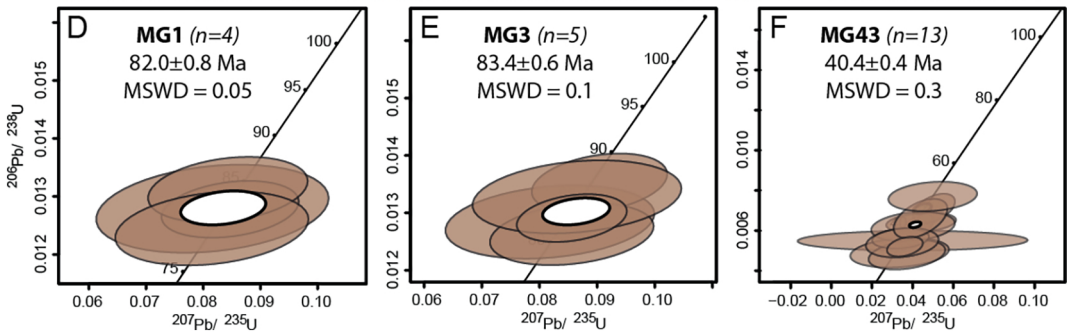


Figure 4

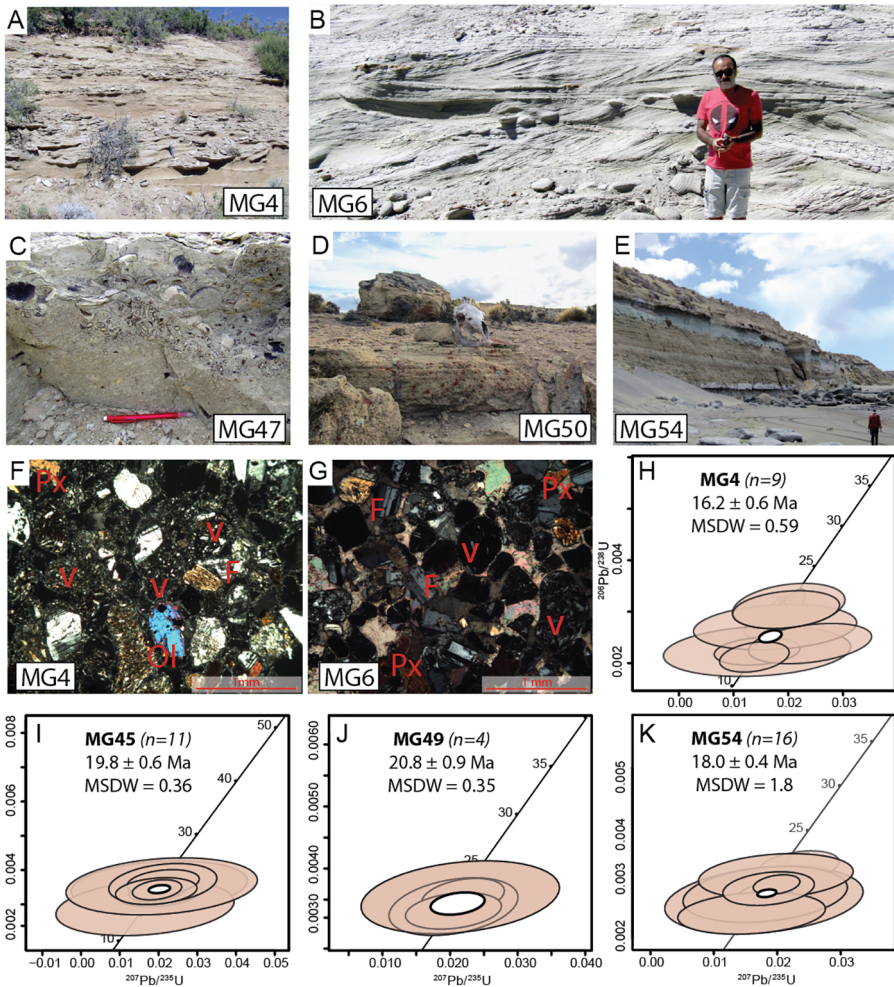


Figure 5

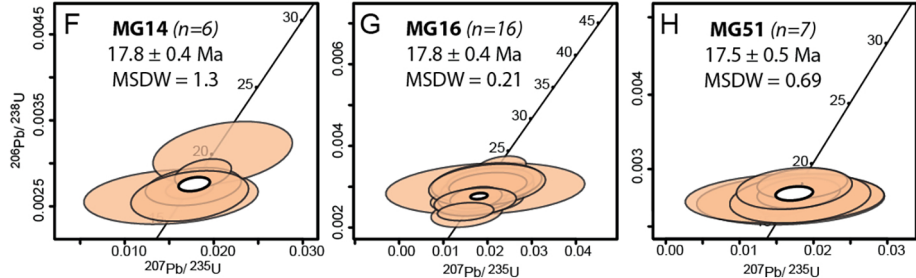
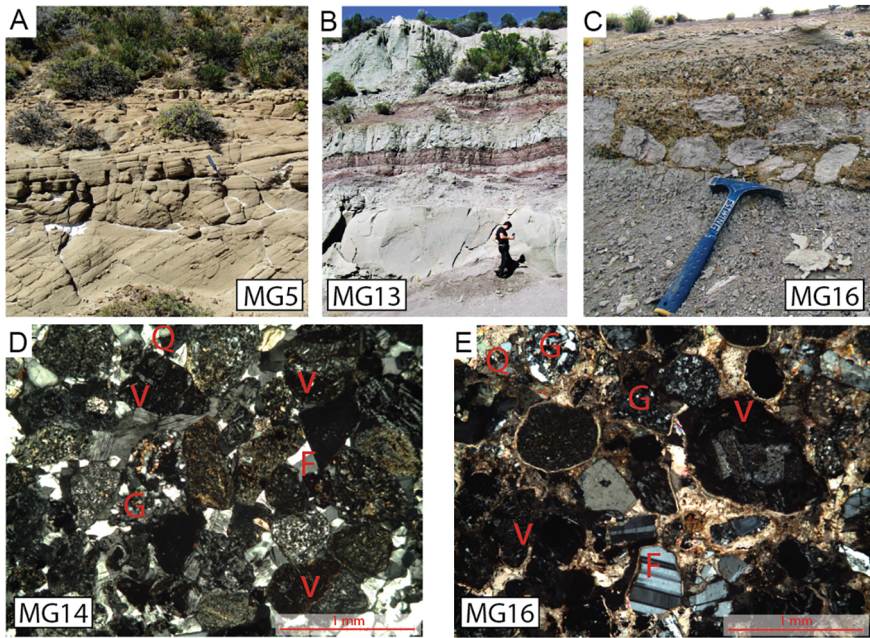


Figure 6

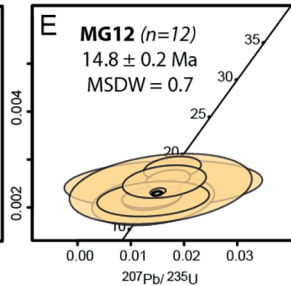
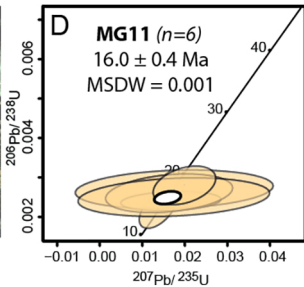
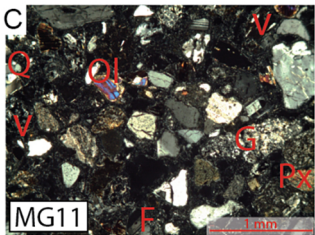


Figure 7

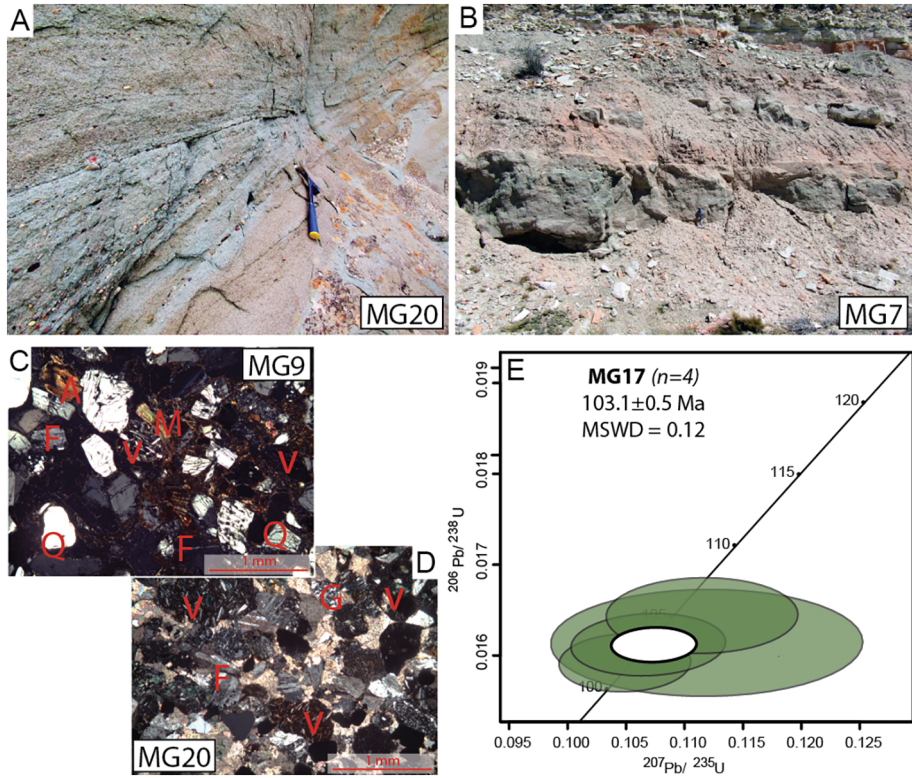


Figure 8

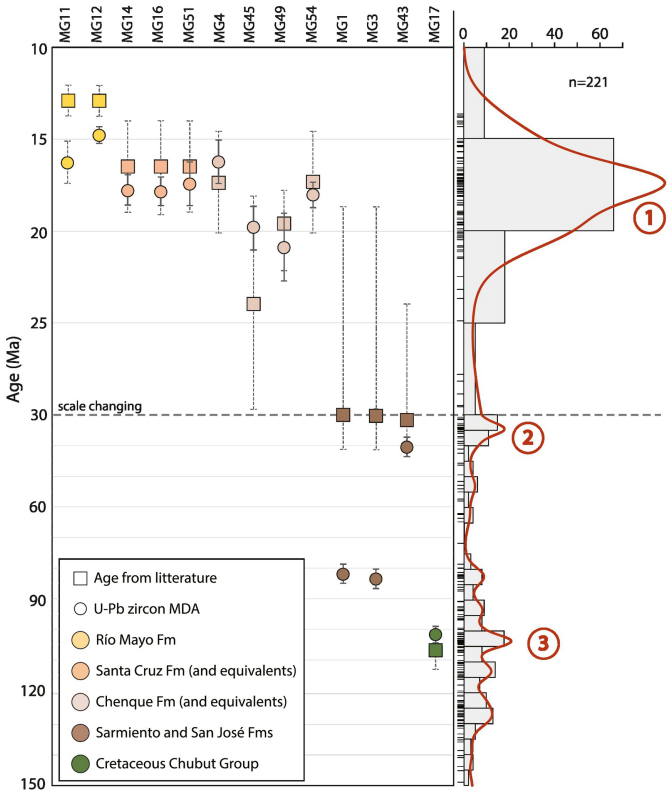
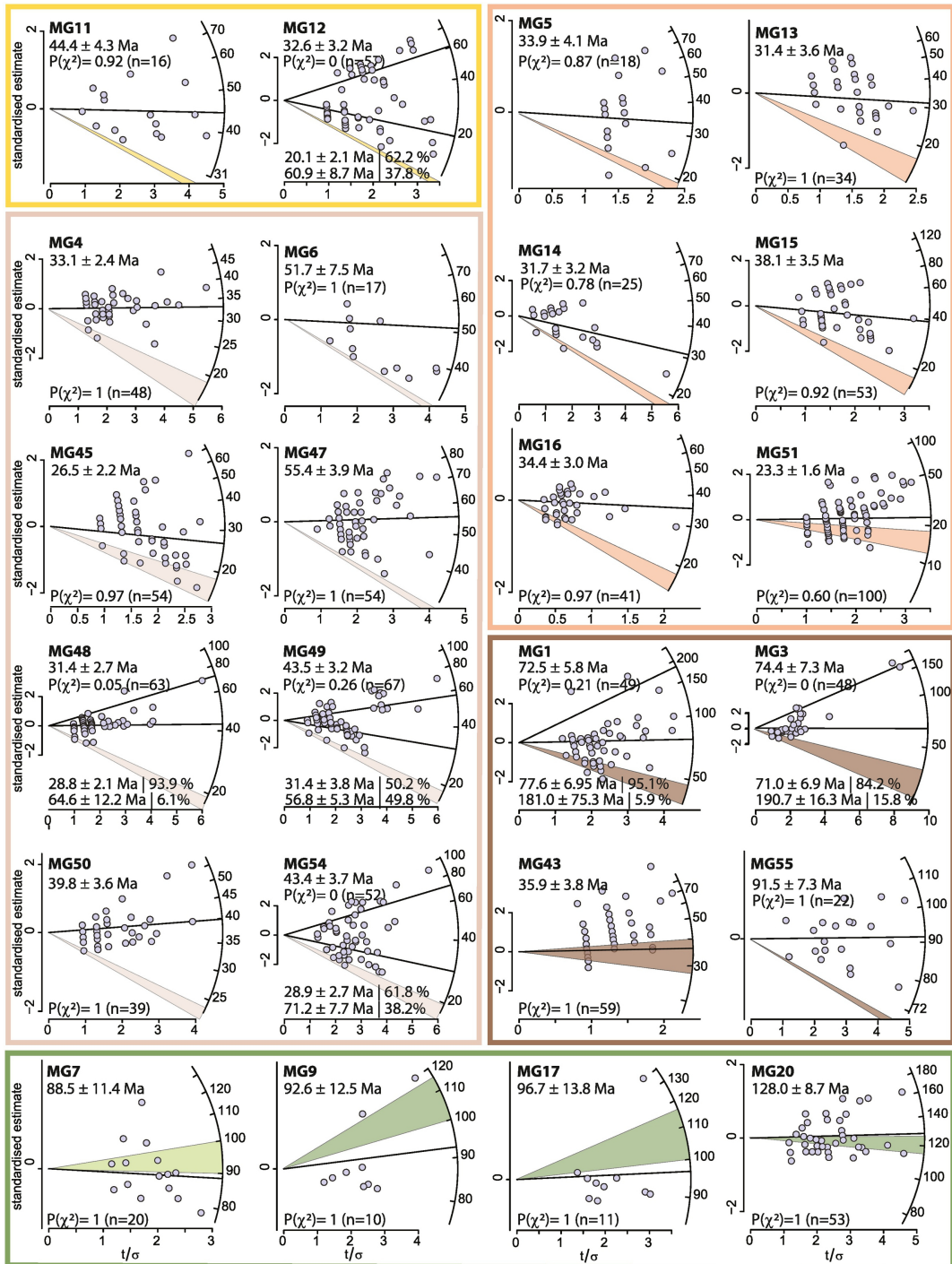


Figure 9



- Single-grain age from different sedimentary formations:

Deposition time:

- | | |
|--|--|
| Late Miocene (Río Mayo Fm) | Late Eocene (Sarmiento, San José Fms) |
| Early-middle Miocene - cont. (e.g., Santa Cruz Fm) | Late Cretaceous (Bajo Barreal Fm) |
| Early Miocene - marine (e.g., Chenque Fm) | Early Cretaceous (Matasiete, Castillo Fms) |

Figure 10

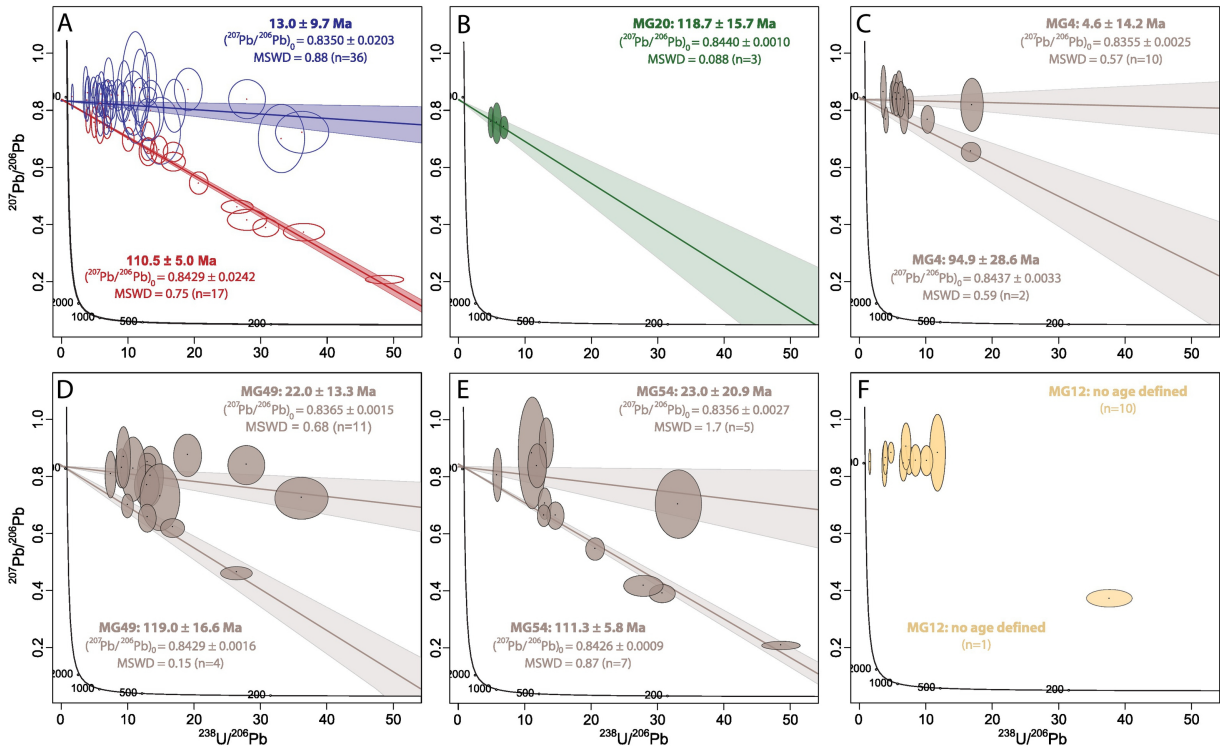


Figure 11

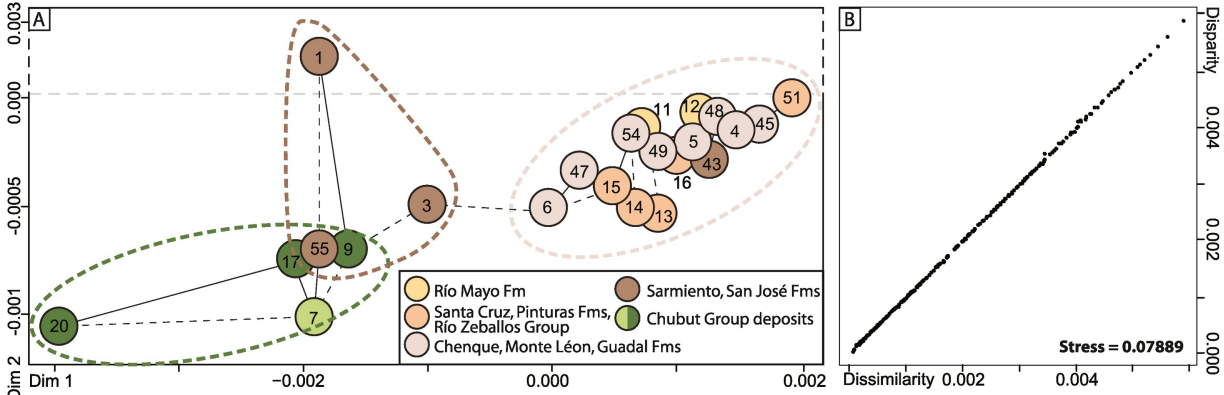


Figure 12

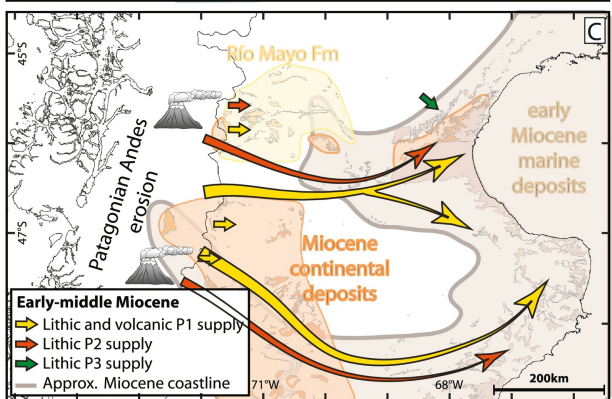
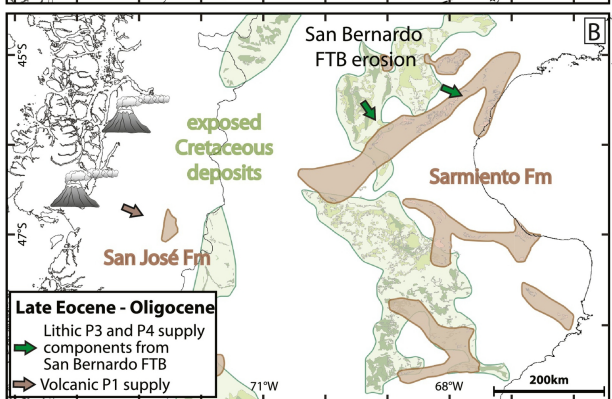
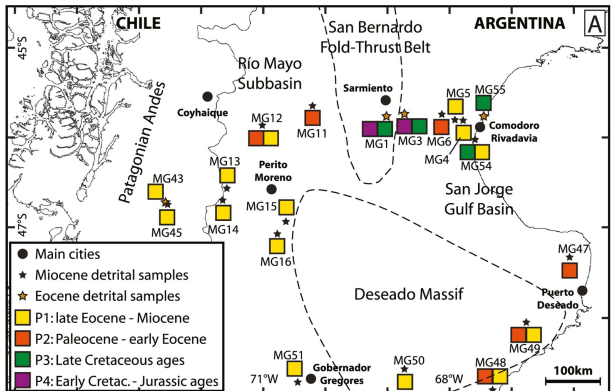


Figure 13